# Towards Dual-Isotope Entangling Gates for Trapped-Ion Quantum Computing

by

Yvette de Sereville

A thesis
presented to the University of Waterloo
in fulfillment of the
thesis requirement for the degree of
Master of Science
in
Physics (Quantum Information)

Waterloo, Ontario, Canada, 2022

## Author's Declaration

This thesis consists of material all of which I authored or co-authored: see Statement of Contributions included in the thesis. This is a true copy of the thesis, including any required final revisions, as accepted by my examiners.

I understand that my thesis may be made electronically available to the public

## Statement of Contributions

Yvette de Sereville is the sole author of Chapters 1, 2, 4 and 5. The content in these chapters were not written for publication. Chapter 3 consists in part of material written for publication.

**For the research in Chapter 2:** This work was conducted under the supervision of Professor Crystal Senko at the University of Waterloo and the Institute for Quantum Computing. Yi Hong Teoh wrote the code used in this chapter to calculate the motional mode spectra, which was updated for the purposes of dual-species ion chains through discussions between Yi Hong Teoh and Yvette de Sereville. Dr. Virginia Frey contributed to the early stage development of simulating MS gates. The simulations of spin-dependent forces shown in this chapter were developed by Yvette de Sereville. This work benefited from discussions and collaboration with Noah Greenberg and Dr. Virginia Frey. Yvette de Sereville performed all of the simulations and analyses shown in this chapter. Yvette de Sereville is the sole author of the content of this chapter.

**For the research in Chapter 3:** This work was published in the journal Physical Review A. This work was conducted under the supervision of Professor Crystal Senko at the University of Waterloo and the Institute for Quantum Computing. Brendan M. White and Pei Jiang Low developed and built much of the experimental infrastructure to be able to conduct the research that went into this paper before the beginning of this thesis research. Yvette de Sereville is responsible for the collection and analysis of all of the conditioning characterization data presented in this chapter. Pei Jiang Low assisted with running and supervising some of the data collection for this chapter with Yvette de Sereville's guidance. The manuscript was written by Brendan M. White with input from Yvette de Sereville on the conditioning characterization results and figures, Pei Jiang Low, Dr. Matthew Day, Noah Greenberg, Richard Rademacher and Professor Crystal Senko. Yvette de Sereville is the sole author of this chapter, with some additional figures included from the publication for completeness.
[48] Brendan M. White, Pei Jiang Low, Yvette de Sereville, Matthew L. Day, Noah Greenberg, Richard Rademacher, and Crystal Senko. Isotope-selective laser ablation ion- trap loading of 137Ba+ using a BaCl2 target. Physical Review A, 2022.

**For the research in Chapter 4:** This work was conducted under the supervision of Professor Crystal Senko at the University of Waterloo and the Institute for Quantum Computing. Dr. Matthew Day developed the initial project bring-up plans to implement $^{137}$Ba$^{+}$ qubits in the laboratory described in this chapter based off of [10]. These plans were further refined by the team through discussions between Yvette de Sereville, Brendan

M. White, Pei Jiang Low, Dr. Matthew Day and Professor Crystal Senko. The product of these project design and planning discussions is summarized in this chapter. All of the experimental implementation presented in this chapter was done by Yvette de Sereville, under the guidance of Pei Jiang Low and Brendan M. White. All of the analysis presented in this chapter was performed by Yvette de Sereville. Yvette de Sereville is the sole author of the content in this chapter.

# Abstract

Entangling gates are essential to the development in the capabilities of any trapped-ion quantum computer. High-fidelity entangling gates have previously been demonstrated on trapped-ion quantum hardware with single species ion chains. We propose a dual-species entangling gate scheme with two different isotopes of barium, namely $^{137}\mathrm{Ba}^+$ and $^{133}\mathrm{Ba}^+$, which would lend itself better to a scalable entangling gate scheme than single or even dual-species architectures. This thesis presents the necessary background to understand entangling gate schemes on trapped-ion systems and how this translates to a dual-isotope infrastructure. The motional mode structure of several dual-isotope ion-chains is calculated and compared against its dual and single species counterparts. It also presents all of the work done to date towards implementing these gates experimentally, including developing an isotope-selective ion-trap loading process and building the necessary infrastructure towards getting $^{137}\mathrm{Ba}$ ions to behave as qubits.

# Acknowledgements

First and foremost, I would like to thank my advisor, Professor Crystal Senko, for giving me the opportunity to work in her group. I would like to thank her for her continued guidance and mentorship throughout the past two years. Thank you for fostering an exciting and collaborative research environment in which questions are always welcome. Despite starting my masters journey a few months into lockdown and the challenges we faced in having to adjust to this new paradigm, Crystal made an enormous effort to ensure we were able to continue making progress. It has been an absolute honour to learn from you over the course of this project. Thank you for encouraging me to finish this thesis within my projected timeline and for all of your insightful advice along the way.

Research is not a solitary endeavor, and I could not have accomplished this much without the support and guidance of my brilliant colleagues. To Pei Jiang Low and Brendan M. White, fellow members of the Qudit Lab, thank you for everything you have taught me throughout my master's. Brendan, thank you for your patience while we generated figure after figure for our paper and Pei Jiang, thank you for answering my every optics question. Thank you both for helping me trap my very first ion! Thank you to Dr. Matthew Day for coming up with the initial experimental designs for our current project and for sharing his insights during his time with the group.

I would also like to thank Noah Greenberg and Dr. Virginia Frey on the QuantumIon team for their helpful discussions and insights as I worked on building simulations for the theory portion of this thesis. I would also like to extend my gratitude to Yi Hong Teoh, both for building the brilliant TriCal platform for our research groups to use, but also for his help in updating the platform for my specific research goals. Thank you!

To all of the other researchers on both the QITI and QuantumIon teams that I unfortunately did not have a chance to collaborate too closely with just due to the circumstances, thank you. Thank you to Nikolay Videnov, Ali Binai-Motlagh and Anthony Vogliano for all of our (virtual) study group sessions as we navigated online courses. A special shout-out to Nikolay for sharing his Inkscape expertise which made generating many of the figures in this thesis so much easier. Thank you!

Thank you also to all of the co-op students that have worked in our lab, both in the past and during these past two years. Thank you for your contributions to the research!

A huge thank you goes out as well to all of the administrative staff in both the physics department at the University of Waterloo and at the Institute for Quantum Computing for their support throughout my master's degree. Thank you for always being so responsive, especially during these challenging times.

Of course, my deepest gratitude to my family for their continued support during my academic journey. I could not have done any of this without you. To my sister, thank you for always reading my work and lending your sharp editing skills. And to my dog, who's been by my side since the first grade, thank you for your companionship every step of the way.

Finally, thank you to my committee members for offering their insights and taking the time to review this thesis, especially given the compressed timeline.

And last, but certainly not least, thank you dear reader, for making it this far into the document. Thank you for taking interest in my work, enjoy!

## Dedication

To the very first ion I ever trapped, wherever you may be now, this one's for you.

# Table of Contents

# List of Figures

# List of Tables

# Chapter 1

# Introduction

## 1.1 Quantum as a Computing Platform

Since their proposal in the mid-20th century, quantum computers have offered a new and exciting approach to quantizing, processing and transmitting information [44]. By using and manipulating the understood behaviour of quantum physics, quantum computers postulate orders of magnitude computational speedups over classical supercomputers, in addition to the possibility of exploring new frontiers of fundamental quantum science [17].

More specifically, using trapped ions to harness the properties of atomic physics to build a quantum computer offers many advantages over alternative approaches. Trapped-ion quantum computers have demonstrated the lowest single-qubit computational gate errors of any quantum hardware platform in addition to other benefits including, but not limited to, very long coherence times and a high potential for scalability [17]; the criteria which could be considered to be three of the most important in evaluating the potential of a quantum device. A robust computing architecture, whether classical or quantum, could be defined as one that consistently makes little to no errors, for extended periods of time, on a platform with the potential to grow and support ever more complex computations. Such behaviour corresponds to the features of gate-error, coherence and scalability, respectively.

The following chapter will detail how the research in this thesis collates work done toward implementing quantum computing with one or more isotopes of Ba+ with the overarching goal of further improving trapped-ion quantum computing architectures.

### 1.1.1 Harnessing Quantum Entanglement

As a property entirely unique to quantum systems, harnessing entanglement as an essential computational resource in quantum hardware may arguably be the defining criteria that really sets quantum computers apart from their classical counterparts [49, 44]. Entanglement in this context being defined as the behaviour of a pair of particles whereby manipulating the state of one particle affects the state of its pair [49, 44].

Entanglement is essential to quantum architectures and plays a key role in many exciting advances in quantum information such as: cryptography, quantum teleportation and quantum error correcting algorithms, the details of which are beyond the scope of this thesis [49, 44]. In other words, many observable quantum speedups are the product of harnessing the property of entanglement [49, 44].

More specifically to trapped-ion quantum computing architectures, the ability to generate entanglement is central to being able to perform any set of algorithms on this platform. This will be discussed further in the subsequent section.

## 1.2 Quantum Logic Gates

Theoretical representations of classical computing systems consist of a series of logic gates arranged into a circuit to express a selected computation. Classical gates take bit-wise inputs and transform them into bit-wise outputs depending on the design of the gate function. There is a specific gate, the NAND gate, which forms a universal gate set from which any classical computation can be expressed by arranging a series of these gates into unique circuit combinations [36].

Analogous to classical logic gates, quantum logic gates can be arranged into unique quantum circuits to perform computations. The circuit representations of quantum logic gates operate much in the same way as their classical counterparts, but instead operate on quantum bits, or qubits [36]. At their most fundamental level, however, quantum gates consist of unitary operators which act on input quantum states [36].

### 1.2.1 Multi-Qubit Entangling Gates

It has been previously demonstrated that entangling gates, in conjunction with single qubit gates, form a universal gate set with which it is possible to model any quantum algorithm [35]. Hence, the reason that being able to generate entanglement effectively on trapped-ion infrastructures is paramount to its scalability. A quantum entangling gate takes two qubits and entangles them.

The simplest way to generate a maximally entangled quantum state, more commonly referred to as a Bell state, is by combining a *Hadamard* and a 2-qubit *Controlled-Not*, or *CNOT*, gate [36] as follows, with qubit$_0$ and qubit$_1$ being in either computational basis states, $|0\rangle$ or $|1\rangle$:

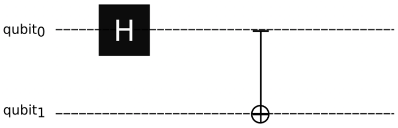

Figure 1.1: Entangling quantum circuit. Adapted from [36]

The output of this entangling quantum circuit, is one of four maximally entangled quantum states (Bell states) between qubit$_0$ and qubit$_1$, depending on their input states [36].

### 1.2.2 Trapped-Ion Quantum Computing

This thesis will focus specifically on trapped-ion quantum computers as a hardware for implementing these quantum gates. As discussed, trapped-ion quantum information (TIQI) systems have previously been established as a good platform for quantum computation with long demonstrated coherence times and high fidelity quantum gates [42].

However, like many other quantum computing implementations, scalability is still a primary challenge for TIQI platforms [42]. Scalability is defined in this context as scaling the number of gates (dual-isotope entangling gates). This, in turn, would also scale the number of ions/qubits, however its primary benefit would be to scale the complexity of the algorithms that could be run on such a platform [43, 22, 14]. An increase in the number of gates would aid in mitigating motional heating during gate cycles by relying on sympathetic cooling methods to reduce the motional excitations in the chain [43, 22, 14]. This will be discussed further in subsequent sections and in detail in Chapter 2.

One key feature in making scalable TIQI architectures possible is how reliably information can be transmitted to/from/between the ions themselves without introducing unnecessary decohering processes [16]. For these reasons, work towards implementing dual-isotope ion-chains would greatly improve the scalability factor of TIQI platforms by introducing new capabilities to execute cooling and measurement operations alongside algorithms, concurrently [14]. Co-trapping a second isotope would allow for mid-circuit measurement and reset (MCMR) operations with limited decoherence introduced from scattering, by interleaving which operations (ie. measurement, & reset) are performed on which subset of isotopes/qubits [14]. MCMR techniques are integral to many error-correcting protocols and measurement-based algorithms, thus a TIQI platform's ability to scale for various applications rests on its ability to synchronously execute universal gate sets (ie. entangling gates) and measurements.

### 1.2.3 TIQI Entangling Gates

As a fundamental pillar of quantum computing technologies, being able to reliably produce entangled states is an important building block for scaling TIQI architectures [16]. TIQI entangling gates operate by transmitting information between ions, whereby the shared motional states between a pair of ions acts as a bus to entangle their electronic (or qubit) states as so [16] (more on this in Chapter 2:

$$|\text{qubit}\rangle \otimes |\text{motional}\rangle \tag{1.1}$$

The most commonly used technique to implement an entangling gate scheme on TIQI architectures is known as the Mølmer-Sørensen (MS) gate and was first proposed in 1999 as an alternative to the Cirac-Zoller CNOT gate (CZ gate) [7]. MS gates have the advantage of not needing the qubits to be in their motional ground states and they do not require individually addressing each ion to produce the resulting entanglement [7]. The MS scheme is the one we will be using to implement the entangling gates discussed in this thesis.

More generally, TIQI entangling gates also have the added benefit of not being limited to nearest neighbor interactions, meaning it is possible to entangle any two qubits in an ion-chain [41].

From a hardware implementations standpoint, the goals are to be able to successfully co-trap various isotopes of barium, address and work with each isotope as a functional qubit and then eventually entangle them. These goals form the basis of this thesis and will be discussed at length in each chapter.

### 1.2.4 Dual-Type Entangling Gates

The specific approach that will be discussed in this thesis to achieve these goals is to introduce a second species to our ion traps to build what we will coin *dual-type* entangling gates. In the context of this document, *dual-type* entangling gates refer to entangling gates between two qubits of different ion species. More specifically, we will discuss the benefits of using two isotopes of a single species over two distinct species. However, *dual-type* will be used to refer to the general group of gates that encompasses both of these approaches.

While dual-type entangling gates between two different species of ions have been previously experimentally implemented, some work has also been done towards two isotopes of the same species with different isotopes of Yb. However, the design of a dual-isotope entangling gate between $^{137}\text{Ba}^{+}$ and $^{133}\text{Ba}^{+}$ is novel to this thesis [41, 42].

## 1.3 Dual-Isotope TIQI Entangling Gates

As one of the primary building blocks of any computer, a universal set of logic gates allows for any computation to be performed on a given platform. Hence, it could be argued that improving the gate capabilities of a given computer hardware architecture would be paramount in improving the performance and subsequently, the scalability of said architecture [42, 36, 7]. Dual-isotope architectures offer just that.

Although implementing a dual-type entangling gate would present challenges over its single-species counterpart, dual-type gates offer significant trade-offs in cooling and MCMR, that would greatly benefit the overall performance of a TIQI platform. These trade-offs will further be investigated in the subsequent section. This section is dedicated to bridging the gap between the theoretical and experimental results presented in this thesis.

### 1.3.1 Dual-Type vs. Single-Species

Single-species entangling schemes have long been demonstrated in the TIQI research community to great effect [30, 41, 39, 25]. However, single-species architectures don't lend themselves well to simultaneously perform quantum gate operations and any dissipative circuit processes, such as cooling, measurement or state reset [14]. In other words, single-species chains make it difficult to actively cool, for example, and perform entangling operations simultaneously. This is predominantly due to the phenomenon of crosstalk between ions, introduced by the photon scattering either emitted by a neighboring ion or from the cooling/measurement/optical pumping (reset) beam itself [14]. This would pose a challenge if we wanted to, say, measure a subset of qubits while performing gate operations on a subset of others within the same ion chain. Especially as the number of qubits, or ions, scales, the inter-atomic spacing between individual ions in a chain decreases, thus making individual addressing even more challenging and increasing the possibility of crosstalk [17, 24].

Introducing a second species to the chain mitigates these issues by also introducing a detuning between the frequencies necessary for any gate operations versus dissipative processes. This, in turn, would limit the probability of crosstalk between those two processes, thus limiting the potential for decoherence.

### 1.3.2 Dual-Type vs. Other Architectures

There exist other proposed architectures of course that have been put forth with the goal of mitigating the crosstalk issue.

One of these architectures is the *omg* blueprint architecture, which consists of exploiting long-lived metastable states in certain ion species as an ‘effective’ secondary species [3]. This would isolate different qubits from scattered light when trying to address others. Whereas the *omg* architecture does have the added benefit of only having a single-species ion-trap loading requirement, transferring qubits into these metastable states to protect them from scattering does add additional operations to a quantum algorithm we would want to execute. Furthermore, *omg* qubits would require very precise spatial addressing of the ions within a chain, so as not to decohere any of the others, which becomes more challenging as the number of ions (qubits) in the chain scales.

An alternative approach involves moving different subsets of qubits in the chain to different physical locations via shuttling [24]. Such a design would typically involve a segmented trap with individually-addressable electrodes to mediate their movement [17, 24]. Shuttling would physically isolate a subset of measurement or ancilla qubits from the rest of the chain, where other gates or operations might be in progress. Shuttling, however, does introduce another source of heating to the trap, which does contribute to unwanted decoherence. An additional shuttling step would also introduce additional complexity in executing a quantum algorithm, thus increasing computing times.

### 1.3.3 Dual-Isotope vs. Dual-Species

Whereas a dual-species architecture (ie. a mixed Ba/Yb chain [42]) would offer greater diversity between the underlying atomic structure and hence, increase the detunings between addressing frequencies, our proposed dual-isotope platform offers two primary benefits over its dual-species counterpart. Firstly, dual-isotope experiments require fewer lasers to address all of the necessary transitions due to the similarities between the two atomic structures, thus simplifying the optical engineering, the design of which will be discussed in Chapter 4. Secondly, due to the smaller mass difference, $\delta$m, between different isotopes of the same species, the motional mode structure of a dual-isotope chain lends itself more favourably to entangling operations and cooling protocols than its dual-species counterpart. The latter benefit will be thoroughly investigated in Chapter 2.

### 1.3.4 From Theory to Experiment

All of the work described in this thesis was implemented with the ultimate goal of implementing dual-isotope entangling gates on a trapped-ion quantum platform using two different isotopes of barium, namely $^{133}$Ba$^+$ and $^{137}$Ba$^+$. As will be seen in Chapter 2, the first step in being able to implement an entangling gate between two ions is calculating and understanding the motional mode structure of these two isotopes within a trapped-ion chain. Experimentally, the first step was to be able to load these two isotopes of barium reliably into the trap, by implementing an isotope-selective loading scheme, discussed in detail in Chapter 3. Finally, there is a lot of infrastructure that had to be designed and implemented in the laboratory in order to be able to manipulate these two isotopes of barium, starting with making $^{137}$Ba$^+$ behave as a qubit. Chapter 4 focuses on the bring-up of the experimental infrastructure related to this.

#### Why Ba$^+$?

The research that went into the decision to pursue barium ions as our choice of qubit is beyond the scope of this thesis. However, a summary of the motivation for Ba$^+$ as our qubit of choice will be presented here, with a further study in [4, 28, 29].

There are not very many elements with two available isotopes which both have non-zero nuclear spin, thus already narrowing the choice to Ba$^+$ and Yb$^+$ as the primary qubit candidates [29]. Non-zero nuclear spin is characteristic of magnetic field insensitive atomic transitions, which are greatly beneficial towards building a stable qubit [29]. Nevertheless, as per [29], barium ions are the better choice to achieve the longer term goal of using them as qu**d**its (vs. qubits), due to their available long lifetime metastable state and visible wavelength transitions, thus simplifying the experimental infrastructure necessary to work with this qubit [29].

#### Looking Ahead

Looking forward, for this project near-term, the goal is to be able to finish implementing the architecture described in Chapter 4 and perform Rabi flopping experiments with $^{137}\text{Ba}^{+}$ qubits, which we are actively in the process of doing. Longer-term, we want to be able to implement dual-isotope entangling gates with these $^{137}\text{Ba}^{+}$ qubits, with the even longer term goal of performing qudit-qudit entangling gates with the above infrastructure, as per [29, 28].

## 1.4 Thesis Outline

### 1.4.1 From Theory to Experiment

#### Theory

**Chapter 2**: this chapter describes the theory behind implementing entangling gates on trapped-ion quantum computing systems and how this theory is modified to accommodate for entanglement between two ions of different species. More specifically, this chapter will explore the specific case of entangling two different isotopes of barium, $^{137}\text{Ba}^{+}$ and $^{133}\text{Ba}^{+}$. This involves investigating the motional mode structure of dual-isotope ion chains with various compositions.

#### Experiment

Chapters 3 and 4 focus on the steps towards the long-term goal of experimental implementation of dual-isotope entangling gates.

**Chapter 3**: discusses an optimal protocol developed to deterministically load each of these barium isotopes into the ion trap, by selectively loading a given barium isotope.

**Chapter 4**: focuses on the experimental infrastructure we're in the process of building to address $^{137}\text{Ba}^{+}$ qubits, including the relevant atomic optics to achieve state preparation and measurement with this isotope, two essential building blocks of a trapped-ion quantum device.

# Chapter 2

# Dual-Isotope Ion Chains

## 2.1 Introduction

High-fidelity (fidelity >0.99) two-qubit entangling gates have already been extensively demonstrated with **single-species** chains on trapped-ion quantum computing hardware [7]. However, in recent years, there has been a push to investigate and implement mixed-species ion chains as a potential approach towards scaling up the functionalities of trapped-ion architectures [43]. As discussed in Chapter 1, scaling remains one of the primary challenges of TIQI architectures, like many other quantum computing platforms [20]. However, specific to trapped-ion hardware, scaling is limited by the ability to perform mid-circuit measurement (MCMR). This chapter will discuss how this overall goal translates to our more specific goal of implementing dual-isotope entangling gates with two different isotopes of barium, namely $^{137}\text{Ba}^+$ and $^{133}\text{Ba}^+$.

### 2.1.1 Dual-Species Ion Chain Architectures

A few trapped-ion quantum information groups have demonstrated dual-species chains of ions already and even fewer have investigated dual-isotope chains with various species of ions to try and address this challenge [7, 43, 20, 6, 42]. There are also benefits related specifically to minimizing decoherence of the qubit states that come with introducing a second ion species to the trap; these benefits will be discussed at length in the subsequent sections.

### Minimizing Crosstalk

A primary benefit of introducing a second species to the trap is eliminating crosstalk between communication and memory qubits [42]. Since, ideally, all ions in a single-species trapped-ion chain are identical (in their electronic structure and otherwise), any subset of ions in a single-species chain could act as either communication or memory qubits. However, since ions are also typically addressed through exciting transitions in their electronic structure, this interchangeability comes with the downside of crosstalk errors introduced by unwanted coupling between identical communication and memory qubits. This could occur, for example, when trying to address a communication qubit but also inadvertently addressing the exact same transition in a memory qubit. Since both qubits are electronically interchangeable, a memory qubit could decohere by absorbing a stray resonant photon [7]. Decoherence could also occur if memory qubits were to absorb re-emitted photons by cooling ions [7]. Crosstalk thus presents a significant challenge in being able to probe any quantum circuits on this platform while simultaneously running any algorithms [42].

Crosstalk errors could be mitigated by introducing a second species to act as either the communication or memory qubit, thus eliminating the interchangeability between the two types of qubits [42, 7]. It is important to pick a second species with transitions that can be addressed that are also far detuned from those of the first in order to minimize the probability of unwanted absorption [7]. However, dual-species chains present their own set of challenges as well, owing to the mass difference between the two species of ions which will be discussed further in the subsequent section on sympathetic cooling considerations [7].

### Sympathetic Cooling

In any trapped-ion quantum infrastructure, cooling is an important part of the experimental cycle in order to minimize motional heating of the system, and thus improve overall performance [7]. However, traditional cooling processes, such as Doppler cooling, involve scattering photons off of the cooling ions, which inherently make them decohering processes [7]. Therefore, direct application of traditional cooling techniques are not really an option for memory qubits [7]. Furthermore, using a cooling ion of an identical species could increase the probability of crosstalk errors, as discussed above.

To address this challenge, a second species could be introduced into the trap for the purposes of cooling memory qubits [20]. The second species would couple to the first via their shared motional modes [7]. Thus, a second species with a similar mode structure would be ideal to fully harness the power of sympathetic cooling protocols. As will be seen in later sections (see Figures 3.3), similarity in the mode structure between ion species is correlated to their mass difference. Thus, whereas single species chains would lend themselves best to sympathetic cooling schemes, their interchangeability presents a hindrance in performing MCMR.

#### Dual-Species Ion Chains are the Answer

Unwanted motional heating of the ions (qubits) as well as crosstalk are both significant contributors to reduced computational performance [20]. In other words, they can both affect the quality of a MCMR. This section will discuss why an answer to these collective challenges is therefore using dual-species ion chains instead [42].

### 2.1.2 Dual-Isotope vs. Dual-Species

To begin, using an isotope as the second species in the ion trap instead of an entirely different species would provide even further improved sympathetic cooling of the system [43]. As discussed, by harnessing sympathetic cooling as a part of our proposed architecture, we can harness the benefit of limiting other forms of cooling, which are inherently decohering processes. However, the effectiveness of sympathetic cooling is dependent on the oscillatory behaviour of the ion chain, known as its motional mode structure, which is in turn, impacted by the chain composition. Thus a further study of how introducing a second isotope plays into this behaviour was necessary, and is the focus of the next section of this chapter.

#### Motional Mode Structures of Ion-Chains

The ions in our trap are confined to a Paul trap, which consists of four rods with an rf voltage applied and two dc end cap needle electrodes to confine the ions along both the radial and axial directions in an effective quadropole field (see [4, 28] for further derivations theoretical details). However, the ions do still oscillate periodically through their equilibrium positions as a result of Coulomb interactions between the ions [23]. The number of motional modes of a system scales proportionally with the number of ions, $N$. Each motional mode has an associated frequency, $\omega_m$ and motional participation vector, $b_{im}$, where $m$ and $i$ are the motional mode number and ion label, respectively. Typically, as well as in this thesis, the convention is to number the ions from left to right, as per Figure 2.1. The motional mode frequency, $\omega_m$, corresponds to the frequency at which the chain will oscillate periodically across its equilibrium position. The motional mode participation vector, $b_{im}$, corresponds to how much each ion is participating in the mode (see Figure 2.1). The ions are free to oscillate in all three coordinate directions, (x,y,z). The x,y-modes are typically referred to as the transverse modes, whereas the z-modes is referred to as the radial mode. The theory motivating the motional mode behaviour of an $N$-length ion-chain will be discussed in-depth in subsequent sections of this chapter.

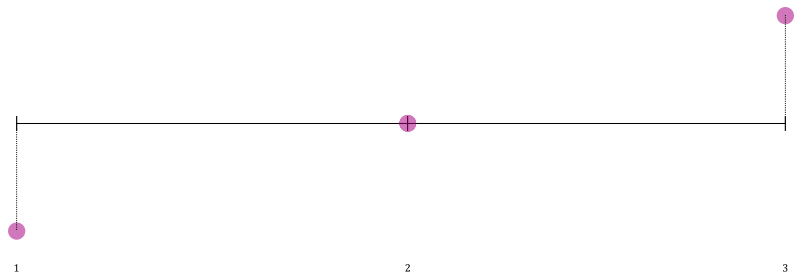

Figure 2.1: Schematic of one of three modes possible for a three-ion chain, often referred to as the "tilt" mode. The pink dots represent individual ions and the dashed lines represent the motional mode participation vectors, $b_{im}$. The equilibrium position of the ions is denoted by the solid line upon which 'ion 2', or the central ion in the chain, rests. Adapted from [30].

### Motional Modes and Sympathetic Cooling

In [43], the author uses the root-mean-square (rms) of the position fluctuation of the ions from their equilibrium positions to characterize the sympathetic cooling process. The rms of this position coordinate is defined as:

$$\langle q_i^2 \rangle = \langle (z_i - z_{i0})^2 \rangle \sum_m \frac{\hbar}{2m_i\omega_m} b_{im}^2 \big(\bar{n}_m + \frac{1}{2}\big) \tag{2.1}$$

where $\bar{n}_m$ is the average phonon occupation number of the $m^{th}$ motional mode, $m_i$ is the mass of the $i^{th}$ ion, $\omega_m$ is the frequency of the $m^{th}$ motional mode, $b_{im}$ is the motional mode participation vector of the $i^{th}$ ion when it's participating in the $m^{th}$ motional mode and $z_{i0}$ is the equilibrium position of the $i^{th}$ ion [43]. Therefore, as evidenced by Equation 2.1, the degree of sympathetic cooling is dependent on the mode structure, both its frequency, $\omega_m$, and mode participation, $b_{im}$, we are trying to leverage it to cool [43].

Based on the derivations presented in [33], the sympathetic cooling rate is then defined as [43]:

$$R_{cooling} = \frac{d}{dt}P(n_m) = \frac{d}{dt}\langle n_m| \rho_m |n_m\rangle \sim \sum_i |\eta_i^m|^2 \tag{2.2}$$

where $n_m$ is the occupation number of the $m^{th}$ motional mode, $\rho_m$ is the density matrix of the $m^{th}$ mode and $\eta_{im}$ is the Lamb-Dicke factor for ion $i$ in mode $m$ and is directly proportional to the motional mode participation vector, $b_{im}$ as we will see in further detail in subsequent sections [43]. The Lamb-Dicke factor, $\eta_{im}$ is both ion and motional mode dependent, and determines how strongly each ion's internal of qubit (spin) states are coupled to its motional, or phonon, states [9]. More specifically, the Lamb-Dicke parameter for a single ion with a single motional mode, $m$, is a ratio defined as:

$$\eta = kx_0 = \frac{2\pi}{\lambda}x_0 \tag{2.3}$$

From an atomic physics standpoint, $\eta_{im}$ thus gives us the information on the ratio between the size of the ion and the wavelength of light, $\lambda$ we use to interact with said ion. $\eta$ is the ratio that helps us understand why lasers give strong spin-motion coupling.

Due to the smaller mass ratio, $\mu = m_1/m_2$, between the two species of isotopes, there is greater participation in the transverse (x,y) modes of the mode structure, thus leading to a higher Lamb-Dicke factor and by extension, making it easier to cool them [43].

## 2.2 $^{137}$Ba$^{+}$:$^{133}$Ba$^{+}$ Dual-Isotope Ion Chains

As motivated in Chapter 1, isotopes $^{137}$Ba$^{+}$ and $^{133}$Ba$^{+}$ were selected over using Yb isotopes instead as per [29] for their visible wavelength transitions and their ability to scale to longer-term qu**d**it infrastructures. In the subsequent sections, we will dive deeper into motional mode structure theory and more specifically, the motional mode behaviour of dual-isotope $^{137}$Ba$^{+}$ and $^{133}$Ba$^{+}$ chains and how this translates to a dual-isotope entangling gate functionality. Since entangling gates on trapped-ion quantum architectures are based on utilizing the shared motional states between the ions, calculating and studying the motional mode structure of our specific barium use-case is the necessary first step towards dual-barium-isotope entangling gates on TIQI infrastructures.

## 2.3 Motional Mode Spectra of Ion Chains

The motional mode spectrum of the ions arises from a combination of the Coulomb force between the ions in the chain and the trapping potential they experience [45]. The subsequent section will discuss how this in turn results in the motional mode behaviour of the ion chain.

### 2.3.1 Theory

The motional or normal modes of a chain of ions consist of the small displacements of the ions that make up the chain away from their equilibrium positions [34]. Thus, the equilibrium positions of the ions must be calculated. Each motional mode also has an associated normal mode frequency at which these small oscillations about the equilibrium position occur as well as an associated normal mode participation vector, which models the strength of the coupling between a given ion in the chain to the corresponding mode, $m$ [34]. The derivation of all of these quantities will be summarized below. Essentially, each normal mode can be thought of as an individual quantum harmonic oscillator [42].

Normal mode participation of an ion chain of length $N$ in an ion trap can be modelled by first considering the Lagrangian of a system of trapped ions [43]:

$$L = \sum_{i=1}^{N} \frac{m_i \dot{\mathbf{r}}_i^2}{2} - U \tag{2.4}$$

where U is the potential energy of the ions in the trap:

$$U = \sum_{i}^{N} \phi(\mathbf{r}_i, m_i) + \frac{1}{2} \sum_{i,j=1 \forall i \neq j}^{N} \frac{e^2}{4\pi\epsilon |\mathbf{r}_i - \mathbf{r}_j|} \tag{2.5}$$

where $\phi$ is the potential energy due to the trap axial confinement and the latter half of the equation is the summation over the Coulomb force between all of the ions, $i$ and $j$ [43].

More specifically, the trap potential can be modelled as follows:

$$\phi_{trap} = \sum_{q=x,y,z} \sum_{i}^{N} \frac{m_i}{2} (\omega_{q,i}^2 q_i^2) \tag{2.6}$$

Due to the Coulomb interaction between the ions, the motion of each ion is coupled to every other in the chain and periodic due to the harmonic potential introduced by the trap [34].

The equilibrium position of the ions is calculated by minimizing the potential energy $U$ of the system along each of the directions of the trap, $\partial U/\partial q_i = 0$ where $q$ is the directional index, $[x, y, z]$ and $i$ is the ion index [42].

By then Taylor expanding the above Lagrangian around the equilibrium positions of the ions [42]:

$$L \approx \frac{1}{2}\Big(\sum_{i=1}^{N} m_i \dot{q}_i^2 - \sum_{i,j=1}^{N} V_{i,j} q_i q_j\Big) \tag{2.7}$$

where:

$$V_{ij} = \frac{\partial^2 U}{\partial q_i \partial q_j} \tag{2.8}$$

is evaluated at the equilibrium positions of the ions [42].

The associated Lagrange equations of motion for the system are then [42]:

$$\Sigma_{i=1}^{N} V_{ij} b_{im} = \lambda_m m_i b_{im} \tag{2.9}$$

where the normal mode frequency is:

$$\lambda_m = {\omega_m}^2 \tag{2.10}$$

with associated normal mode vector: $b_{im}$.

### 2.3.2 Simulating the Motional Behaviour of Dual-Isotope Chains

To be able to implement dual-isotope entangling gates in a selected chain of ions, we must first calculate the motional mode frequencies and normal mode couplings of each of the ions in a selected chain composition [42]. As discussed in section **??**, these parameters were calculated using a previously developed trapped-ion calculator package by Yi Hong Teoh [46, 47] and through discussions between Yi Hong Teoh and myself, the package was updated to accommodate for dual-isotope ion chains.

The algorithm used in this section to calculate the motional modes is the one proposed in [47] and further described in [46]. However, the package was updated when we noticed a discrepency between the motional mode frequencies cited in [31], which presents results on a mixed-species chain of $\mathrm{Ca}^+$ and $\mathrm{Be}^+$, and our calculated results. Yi Hong determined that the way we were calculating the trapping strengths in the transverse direction for the second ion species based on the primary trapped species had to be scaled to accommodate for the mass difference between species. The simulation package was updated to reflect the approach of calculating the trap strength of the secondary species according to [31].

### Primary Parameters

The primary parameters that could affect the motional mode spectrum of the ion chain are the following:

- **Chain Length**: the number of radial (x or y) modes scales with the number of ions in the chain, ie. $N = m$.
- **Chain Composition**: introducing a second species into the chain changes the motional mode structure relative to its single-species counterpart.
- **Chain Distribution**: the ordering of the ions in the chain also affects the mode structure, with symmetric configurations producing identical results. Symmetry in this context is defined as symmetry in the ion-chain, in terms of isotopic species. For example, a chain with three ions with 2:$^{137}\mathrm{Ba}^+$ and 1:$^{133}\mathrm{Ba}^+$ with the 2:$^{137}\mathrm{Ba}^+$ located at the ends of the chain would result in the same mode structure if the 2 ions were swapped by the nature of the interchangeability between ions.

These were the three parameters that were varied to investigate the effects on a dual-isotope chain of ions.

### Visualizing the Motional Behaviour of Dual-Isotope Ion Chains

In this section we will look at comparing the motional mode spectrum of dual-isotope chains against both their dual-species and single-species counterparts. More specifically we will consider how the above parameters impact the motional mode participation of each ion for each of the modes in chain lenghths of $N = 3$.

| **Dual-isotopes** | **Dual-species** | **Single species** |
|---|---|---|
| ($^{133}$Ba$^{+}$,$^{137}$Ba$^{+}$) | ($^{133}$Ba$^{+}$,$^{171}$Yb$^{+}$) | $^{137}$Ba$^{+}$ |

Table 2.1: Species pairings used in each of the simulations.

For all of the simulations included in this section, the trapping strengths used were $[\omega_x, \omega_y, \omega_z]/2\pi = [3, 3, 0.7]$ MHz and all plots correspond to the x radial (transverse) modes of the chain, since these are parameters typical for experiment [43, 42]. Furthermore, the transverse modes lend themselves better to sympathetic cooling schemes, as discussed above.

The main takeaway here is that the motional mode participation structure of dual-isotope chains more closely resembles that of single-species chains than dual-species chains does. In dual-species chains, there is little to no participation in the mode structure for all three modes by the second species, thus making sympathetic cooling more challenging. Therefore, we can draw on many of the benefits of a single species chain while pushing on a lot of the functionality (ie. MCMR) that just isn't possible with only a single trapped ion species, while still harnessing sympathetic cooling schemes.

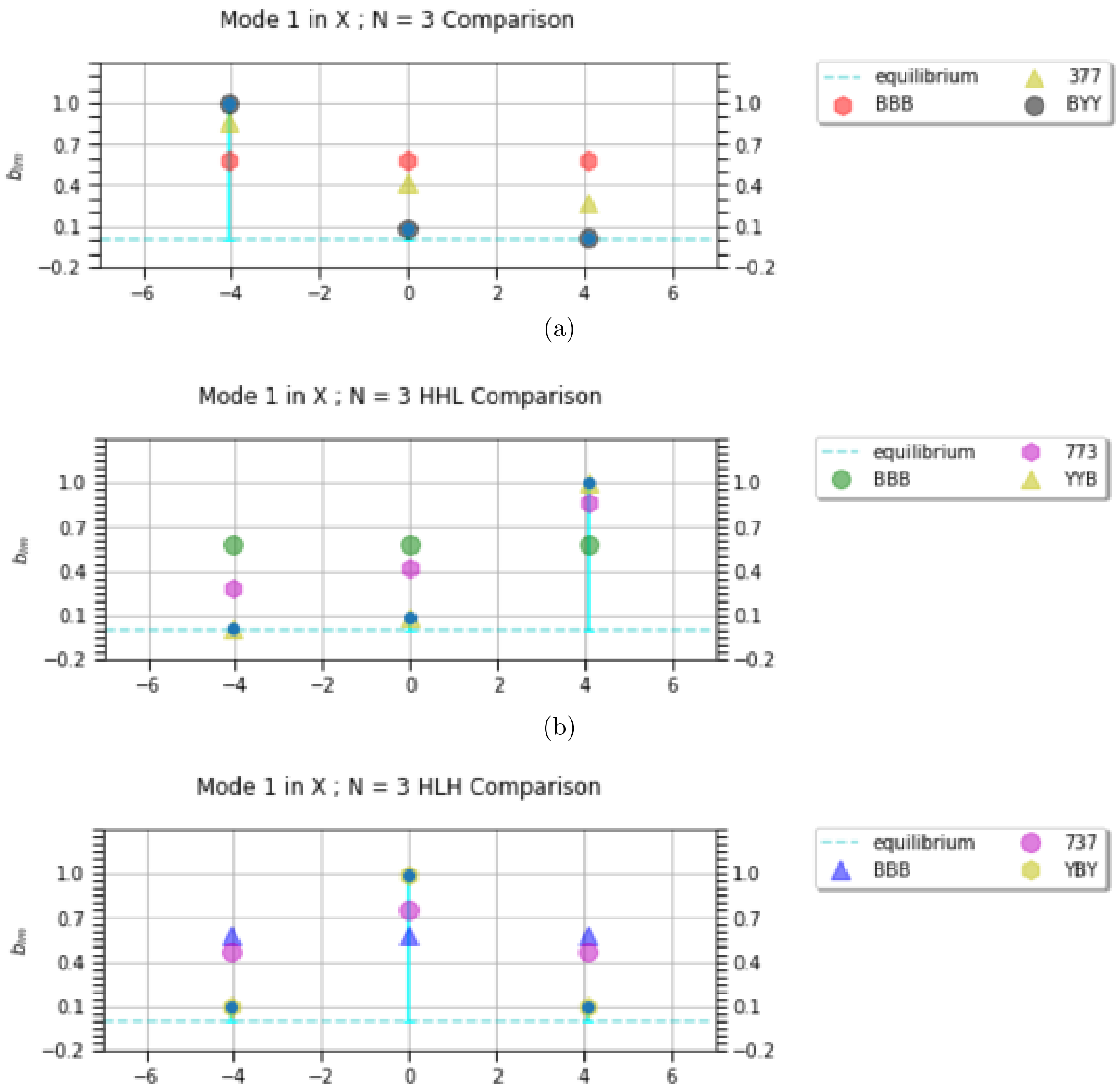

(a)

(b)

(c)

Figure 2.2: Mode structure of mode 1 in an $N = 3$ chain with a single $^{133}$Ba$^+$ introduced to each chain. Plot of motional mode participation vector vs. relative equilibrium ion spacing. All three configurations are represented here, with 'H' referring to the heavier species, $^{137}$Ba$^+$ and 'L' referring to the lighter species $^{133}$Ba$^+$.

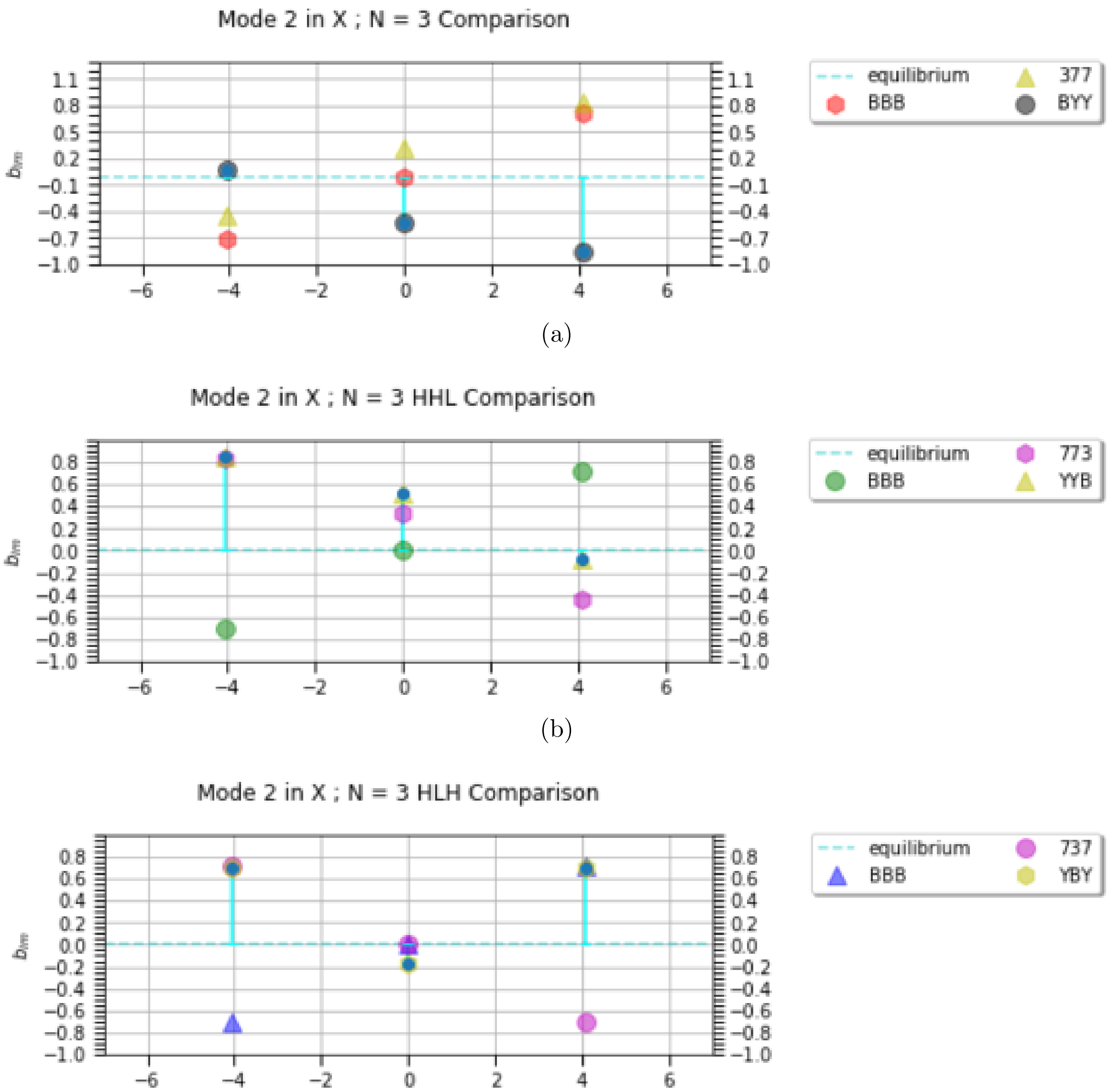

(a)

(b)

(c)

Figure 2.3: All three configurations in Mode 2.

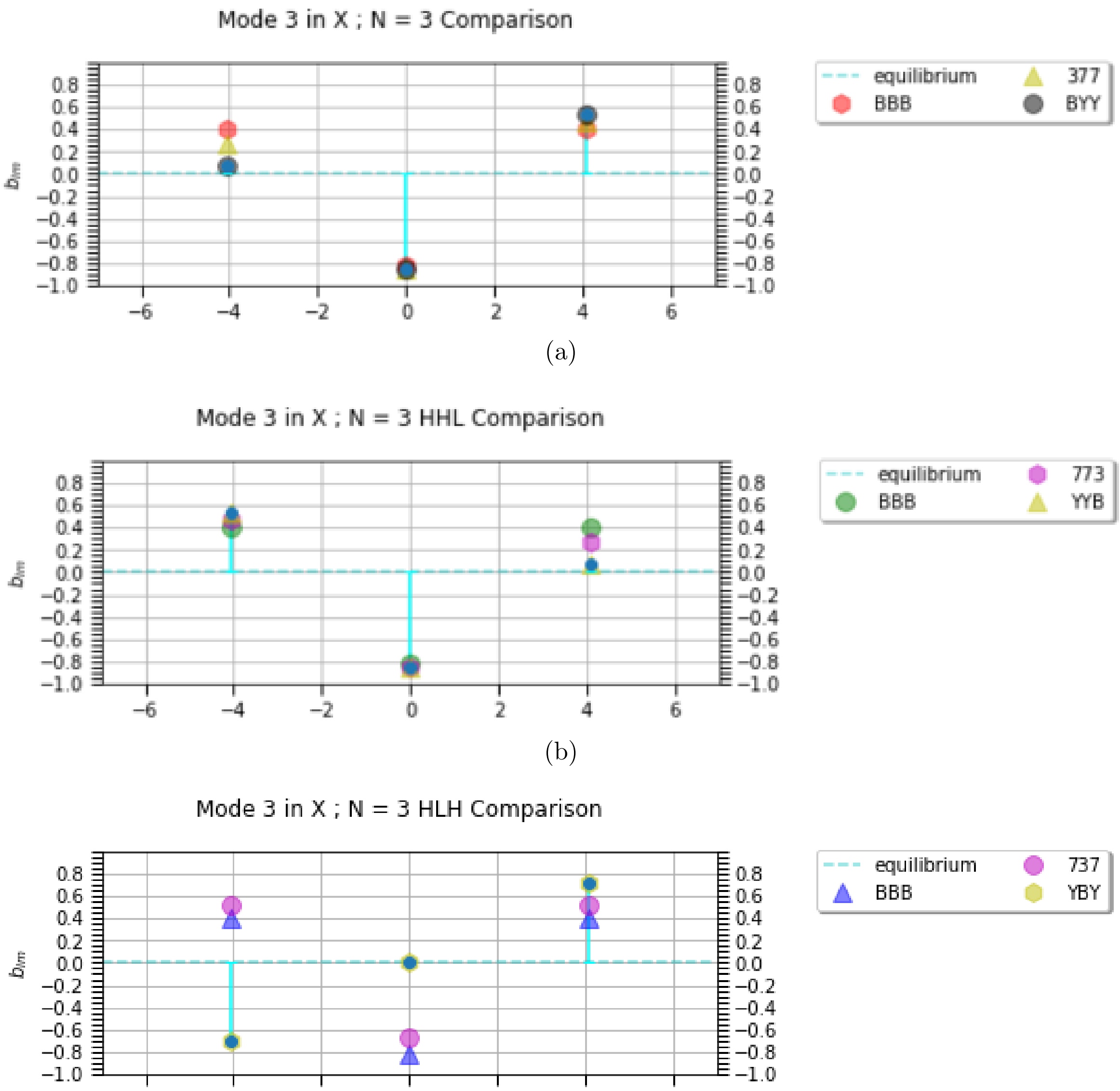

(a)

(b)

(c)

Figure 2.4: All three configurations in Mode 3.

## 2.4 TIQI Entangling Gates

The way entangling gates are implemented on TIQI architectures (and will be on ours) is typically using the Mølmer-Sørensen (MS) entangling scheme [32]. These gates have the highest demonstrated fidelity of any entangling gate implementation [45].

### 2.4.1 Spin Dependent Forces

Spin-dependent forces are the building blocks of MS entangling gates. They are the mechanisms that actually mediate the entanglement between spin (qubit/internal) states of the ions through the coupling of their motional states [15]. As their name implies, the direction of the force depends on the spin state of the ion, as we will discuss further in this section.

In contrast to the previously broadly used Cirac-Zoller scheme [27], using spin-dependent forces to entangle the qubit states of the ions does not require the system to be initialized in its motional ground state [27]. Spin-dependent forces operate by coupling to a specific motional mode of the system [27].

#### Coherent States of the Harmonic Oscillator

Coherent states of the quantum harmonic oscillator (QHO), $|\alpha\rangle$, obey the following relationship:

$$a\,|\alpha\rangle = \alpha\,|\alpha\rangle \tag{2.11}$$

In other words, they are eigenstates of the annihilation operators of a QHO system [27].

Displacement operators are able to "displace" a coherent state in phase-space by:

$$D(\beta)\,|\alpha\rangle = e^{i\mathrm{Im}(\alpha^*\beta)}\,|\alpha+\beta\rangle \tag{2.12}$$

where $D$ is the displacement operator.

Phase-space is the coordinate space defined by the state's position and momentum and $i\mathrm{Im}(\alpha^*\beta)$ is defined as the geometric phase, or the area enclosed by the trajectory of the state in phase-space [27].

Conceptually, it is easiest to discuss how entanglement can be achieved through this gate operation by looking at single qubit entanglement as in [20] and [27].

Spin dependent forces are periodic forces detuned from a selected motional mode frequency that generate periodic trajectories in rotating phase-space.

To implement an entangling gate scheme, a periodic force of the following form is applied, where $\omega_m$ is the frequency of the $m^{th}$ motional mode [27].

$$F(t) = |F|\sin[(\omega_m \delta) + \phi] \tag{2.13}$$

The applied force is spin-dependent because the different eigenstates of the spin operator experience a force in a direction depending on their spin state [27]. This results in the motional states being displaced in phase-space.

In the single ion case, the MS Hamiltonian can be written as [20]:

$$H_{MS} = \frac{\hbar\eta\Omega}{2}(\sigma_+ e^{i\phi_s} - \sigma_- e^{-i\phi_s})(a e^{i\phi_m} e^{-i\delta t} + a^\dagger e^{-i\phi_m} e^{i\delta t}) \tag{2.14}$$

where the spin and motion phases are defined as: $\phi_s = (\phi_r + \phi_b)/2$ and $\phi_m = (\phi_r + \phi_b)/2$, respectively, and $(\sigma_+ e^{i\phi_s} - \sigma_- e^{-i\phi_s})$ is defined as the $\sigma_{\phi_s}$ force [27]. $H_{MS}$ takes the form of a spin-dependent Hamiltonian [27]. The force operates by entangling the spin degree of freedom of the ion with its motional mode [15]. However, the spin and motion become disentangled at the end of the period as long as the phase-space trajectories close and the qubit acquires a geometric phase [15].

A state initialized in the spin up state evolves under this spin dependent force as per Figure 2.5 [27].

The initial state of the ion $|\uparrow\rangle = \frac{1}{\sqrt{2}}(|+\rangle + |-\rangle)|0\rangle$, which evolves in phase space according to the spin dependent force [15]. In the z-basis, which is typically used for measurement, this results in the entangled state $|\uparrow\rangle(|\alpha\rangle + |-\alpha\rangle)/2 + |\downarrow\rangle(|\alpha\rangle + |-\alpha\rangle)/2$ [15]. The periodic behaviour of this entanglement as a function of the applied force in shown in Figure 2.5.

### 2.4.2 Mølmer-Sørensen Entangling Gate Theory

Traditionally used in TIQI is the Mølmer-Sørensen (MS) entangling gate scheme, whereby entanglement is mediated by the collective phonon modes of motion of the ion chain. Experimentally, the MS gate is implemented by simultaneously exciting a pair of ions by red and blue detuned sideband transitions from a selected motional mode of the system [20]. The basis on which these modes are selected will be further discussed in Section 2.4.3. The red an blue sideband detunings are exactly equal and opposite, $\delta_{blue} = \delta_{red}$. This results in a spin-dependent force being applied to the ion.

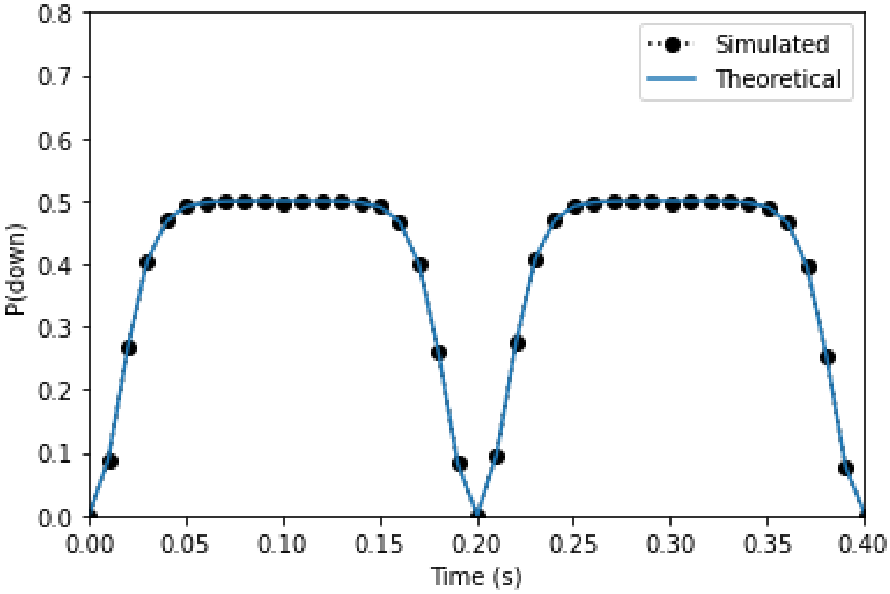

Figure 2.5: Probability of being in the spin down state vs. duration of the spin-dependent force applied to the system. Simulated result adapted from Figure 4.2.3 in [27]

.

A spin-dependent force, as discussed in Section 2.4.1, is applied to the qubits and the direction of the force is dependent on the internal qubit state of the ion [45]. The force drives the motional state of the ion in a given trajectory in phase space, $\alpha(t)$, depending on the value of the detuning $\delta$ of the drive frequency from the motional mode frequency [45]. The area enclosed in phase space by the trajectory of the motional state is proportional to the geometric phase picked up by the qubits [45]. Ideally, to maximize entanglement, we want this geometric phase to be equivalent to $\pi/4$.

This following derivation of the MS Hamiltonian is a general derivation, meaning that it can apply to an arbitrary chain of ions, regardless of length or species composition. The specific parameters of the MS entangling gate that are impacted by the ion chain length and species composition will be discussed in further detail in Section 2.4.3.

Starting from the interaction Hamiltonian for a bichromatic laser field applied to an ion chain (see Appendix A):

$$H_{int} = \sum_{i,m} \eta_{i,m}\Omega_i \Big( a_m e^{-i\omega_m t} + a_m^\dagger e^{i\omega_m t} \Big) \sin(\mu t)\sigma_x^{(i)} \tag{2.15}$$

where:

$$\begin{cases} i \equiv \text{i}^{th} \text{ ion} \\ m \equiv \text{m}^{th} \text{ collective motional mode} \\ \eta_{i,m} = b_{i,m}\delta_k\sqrt{\frac{\hbar}{2m\omega_m}} \\ \mu \equiv \text{detuning from qubit frequency} \end{cases} \tag{2.16}$$

where:

$$\Big\{ b_{i,m} = \text{normal mode transformation matrix} \tag{2.17}$$

which is also the motional mode participation vector from Section 2.3.1

Applying the Magnus expansion, the MS evolution operator can be written as:

$$U(t) = exp\Big(\overline{\Omega_1} + \overline{\Omega_2} + \overline{\Omega_3} + \ldots\Big) \tag{2.18}$$

where:

$$\begin{cases} \overline{\Omega_1} = -i\int_0^t H(t_1)\,dt_1 \\ \overline{\Omega_2} = -\frac{1}{2}\int_0^t \Big(\int_0^{t_1}\Big[H(t_1), H(t_2)\Big]\,dt_2\Big)\,dt_1 \end{cases} \tag{2.19}$$

Substituting $H_{int}$ for $H(t)$ into $\overline{\Omega_1}$:

$$\overline{\Omega_1} = -i\int_0^t \Big(\sum_{i,m}\eta_{i,m}\Omega_i\Big(a_m e^{-i\omega_m t_1} + a_m^\dagger e^{i\omega_m t_1}\Big)\sin(\mu t_1)\sigma_x^{(i)}\Big)dt_1 \tag{2.20}$$

Pulling out the integral for the time-dependent part of Equation 2.20, let the time-independent constant in the equation be:

$$\sum_{i,m}\Big(-i\eta_{i,m}\Omega_i\sigma_x^{(i)}\Big) \tag{2.21}$$

The time-dependent integrals for the motional-dependent raising and lowering operators, respectively are:

$$a_m : a_m \int_0^t e^{-i\omega_m t_1} \sin(\mu t_1) dt_1 \tag{2.22}$$

$$a_m^\dagger : a_m^\dagger \int_0^t e^{i\omega_m t_1} \sin(\mu t_1) dt_1 \tag{2.23}$$

In order to simplify the expression for $\overline{\Omega}_1$, we will define a new quantity, $\alpha_{i,m}(t)$, that will come to be known as the phase-space trajectory, as follows:

$$\alpha_{i,m}(t) \equiv -i\eta_{i,m}\Omega_i \int_0^t e^{i\omega_m t_1} \sin(\mu t_1) dt_1 \tag{2.24}$$

Similarly substituting $H_{int}$ into the commutation relation for $\overline{\Omega}_2$ in the Magnus expansion results in:

$$\Big[H_{int}(t_1), H_{int}(t_2)\Big] =$$
$$\Big[\sum_{i,m} \eta_{i,m}\Omega_i \Big(a_m e^{-i\omega_m t} + a_m^\dagger e^{i\omega_m t}\Big)\sin(\mu t)\sigma_x^{(i)}, \sum_{j,l} \eta_{j,l}\Omega_j \Big(a_l e^{-i\omega_l t} + a_l^\dagger e^{i\omega_l t}\Big)\sin(\mu t)\sigma_x^{(j)}\Big]$$

where:

$$\begin{cases} i, j \equiv \text{ion indices} \\ m, l \equiv \text{motional mode indices} \end{cases} \tag{2.25}$$

By the commutative property of the ladder operators, $a_m$ and $a_m^\dagger$:

$$\Big[a_m, a_l\Big] = \Big[a_m^\dagger, a_l^\dagger\Big] = 0 \qquad \forall\ m, l \tag{2.26}$$

However:

$$\Big[a_m, a_l^\dagger\Big] = \delta_{ml} \qquad \forall\ m, l \tag{2.27}$$

For the $\sigma_x$ operators:

$$\left[\sigma_x^{(i)}, \sigma_x^{(j)}\right] = 0 \qquad \forall\ i, j \tag{2.28}$$

By these properties, pulling out the operators and ignoring the constants for the time being, the two relevant commutation relations are as follows:

$$\begin{cases} \left[a_m e^{-i\omega_m t_1}\sigma_x^{(i)},\ a_l^\dagger e^{i\omega_l t_2}\sigma_x^{(j)}\right] = e^{i\omega_m(t_2-t_1)}\sigma_x^{(i)}\sigma_x^{(j)}\delta_{ml} \\ \\ \left[a_m^\dagger e^{i\omega_m t_1}\sigma_x^{(i)},\ a_l e^{-i\omega_l t_2}\sigma_x^{(j)}\right] = -e^{-i\omega_m(t_2-t_1)}\sigma_x^{(i)}\sigma_x^{(j)}\delta_{ml} \end{cases} \tag{2.29}$$

Therefore, $\overline{\Omega_2}$ in the Magnus expansion then simplifies to:

$$\overline{\Omega_2} = \chi_{i,j}(t)\sigma_x^{(i)}\sigma_x^{(j)} \tag{2.30}$$

where:

$$\chi_{i,j}(t) = \frac{i}{2}\int_0^t dt_1\Big(\sum_m \eta_{i,m}\eta_{j,m}\Omega_i\Omega_j \sin(\mu t_1)\sin(\mu t_2)\big(e^{-i\omega_m(t_2-t_1)} - e^{i\omega_m(t_2-t_1)}\big)\Big) \tag{2.31}$$

Higher orders of the Magnus expansion include terms such as:

$$\Big[H(t_1), \Big[H(t_2), H(t_3)\Big]\Big] + \Big[H(t_3), \Big[H(t_2), H(t_1)\Big]\Big] = 0 \tag{2.32}$$

since:

$$\left[\sigma_x^{(i)}a_m, \sigma_x^{(i)}\sigma_x^{(j)}\right] = 0 \tag{2.33}$$

Therefore the unitary evolution operator simplifies to:

$$U(t) = \exp\big(\overline{\Omega_1} + \overline{\Omega_2}\big) = \exp\Big(\sum_{i,m}\big(\alpha_{i,m}(t)a_m^\dagger + \alpha_{i,m}^*(t)a_m\big)\sigma_x^{(i)} + i\sum_{i,j}\chi_{i,j}(t)\sigma_x^{(i)}\sigma_x^{(j)}\Big) \tag{2.34}$$

The $\alpha(t)$ values in this expression represent the time-dependent trajectory of the motional states in phase-space. For values of $\alpha(2\pi/\delta)$, where $2\pi/\delta$ is the period of the evolution, $\alpha(2\pi/\delta) = 0$ [27]. This means that the phase space trajectories close if we set the gate time equal to an integer multiple of this period, thus resulting in an entirely $\sigma_x\sigma_x$ entangling gate. $\chi$ is the geometric phase accumulated during the displacement in phase space and is equivalent to the area enclosed, as discussed previously.

The following is a truth table of of what an entangling gate should do for spin (qubit) states in a system of two-ions:

| **Initial State** | **Final State** |
|---|---|
| $\left\|\uparrow\uparrow\right\rangle_x$ | $\left\|\uparrow\uparrow\right\rangle_x$ |
| $\left\|\downarrow\downarrow\right\rangle_x$ | $\left\|\downarrow\downarrow\right\rangle_x$ |
| $\left\|\uparrow\downarrow\right\rangle_x$ | $e^{i\phi}\left\|\uparrow\downarrow\right\rangle_x$ |
| $\left\|\downarrow\uparrow\right\rangle_x$ | $e^{i\phi}\left\|\downarrow\uparrow\right\rangle_x$ |

Table 2.2: Truth table for an MS entangling gate for a single mode shared by two ions, where $\phi$ represents the accumulated phase in phase space.

### 2.4.3 Connection to the Motional Mode Spectra of the Ions

Favored, or ideal, modes of a chain to implement dual-isotope entangling gates would be the ones where there is significant participation in the mode by both isotopes in the corresponding chain (see Figures 2.2-2.4).

It is desirable to choose motional modes that have significant motional mode participation for both ions. The participation vector, $b_{i,m}$, is a good measure of this. We want to be able to address both ions without needing to increase the control-field intensity significantly [7]. There is always a limit to the amount of optical power and the range on the beam waist of the addressing system used to communicate with the different sites in the chain.

### 2.4.4 Pulse Sequences

When there is a only a single ion, decoupling from its respective motional mode consists of setting the blue and red sideband frequencies to equal and opposite detunings from the motional frequency. However, when multiple motional modes are involved, in order to decouple from all of the motional modes at the end of the gate time, it would be impossible to set the detunings accordingly to achieve a high-gate fidelity [30, 42]. Therefore, it is necessary to implement pulse shaping techniques that break down the phase space trajectory into several different segments, each with their own duration in order to force the phase space trajectories to close at the end of the gate time [30]. The pulse sequence design would be highly dependent on the mode structure of the chain we are trying to address. This would be the next natural extension of this work.

# Chapter 3

# Isotope-Selective Ion-Trap Loading

## 3.1 Loading $^{137}\text{Ba}^+$ into the Trap

In order to be able to implement dual-isotope entangling gates with $^{137}\text{Ba}^+$ and $^{133}\text{Ba}^+$ ions experimentally, it is important to be able to first produce and load these two isotopes of barium reliably [48].

Three of the primary metrics involved in optimizing the loading process are: the loading rate, defined as the number of ions loaded per ablation pulse, the isotope-loading efficiency, defined as how deterministically a specific isotope, or series of isotopes, can be loaded into the trap relative to their natural abundance, as well as the replicability of the loading process, the latter of which will be the focus of this chapter [48].

### 3.1.1 Laser Ablation Loading Technique

The laser ablation process works by ablating atoms from a $\text{BaCl}_2$ target using high-energy laser pulses. The ablation laser used in these experiments consists of a 532 nm Nd:YAG pulsed laser with pulse widths on the order of nanoseconds [48, 4]. The spot sizes produced on the $\text{BaCl}_2$ target as a result of the pulses interacting with the target surface are on the order of tens of micrometers [48]. The $\text{BaCl}_2$ target itself resides inside our vacuum chamber, which also hosts our ion trap, with the target surface angled towards the trap center so as to maximize the flux of neutral barium atoms into the trap [48].

**Barium Isotope Selectivity**

Once neutral atoms have been ablated from the $BaCl_2$ target surface, the resulting neutral atom flux must then be ionized to produce the desired ions [48]. This is achieved through a two-step photoioionization process, using a 554 nm laser to address the $S_0$ to $P_1$ transition in barium (see Figures 3.1 and 4.1), followed by a 405 nm laser to eject a valence electron from each of them, thus ionizing the barium atoms [48]. The 405 nm laser is aligned 90 deg relative to the 554 nm beam so as to restrict the volume of ionization to the trap center [48]. This particular geometry is desirable because according to the trap design, the trap center also corresponds to the minimum of potential energy of the trapped ions, which subsequently reduces the ion cooling time [48, 28].

The frequency on resonance with the $S_0$ to $P_1$ transition in barium atoms is unique for each isotope of barium [48, 4]. The 554 nm ionization laser frequency can therefore be modulated to be on resonance with each of these unique $S_0$ to $P_1$ transition frequencies, thus selectively ionizing, and subsequently loading, specific isotopes of barium into the trap [48]. In other words, isotope-selective loading is all about setting the 554 nm laser to the correct frequency peak of the desired isotope [48, 4]. With the current experimental infrastructure, it is possible to discern between all of the different isotopes of barium except $^{135}Ba^+$.

The ions produced through this process then crystallize in the trap center to form a trapped-ion chain [48]. The trap architecture consists of a 4-rod Paul trap with approximately 66 V rf voltage on all 4 rods and 5-10 V dc voltage on the end caps, with diagonal rods having opposite polarity for axial and radial confinement, respectively [48].

### 3.1.2 Laser Ablation vs Oven-Loading

Historically, oven-loading was typically used to load ions into an ion-trap. However, for the specific ion species we work with, laser ablation loading presents many advantages over traditional oven-loading techniques [48], in addition to making it possible to load the radioactive barium isotope, $^{133}Ba^+$, into our trap to use for dual-entangling gate purposes [48]. Conventional oven-loading requires a barium metal target, which is not an option for $^{133}Ba^+$ due to its radioactive nature [48]. Ablation loading also requires the use of less material overall and introduces a lower heat load into the trap [48]. Both of these properties help to reduce both the contamination and the subsequent unwanted pressure spikes into the trap [48]. Unwanted heat loading can make cooling the ions more challenging, thus introducing another potential source of decoherence [48]. Ablation is also the faster of two

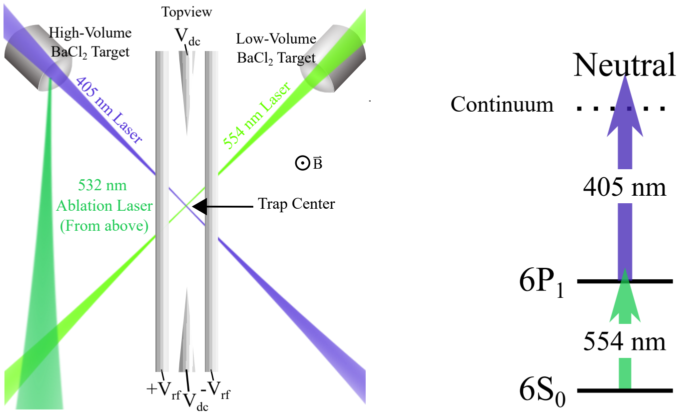

(a) (b)

Figure 3.1: (a) Experimental setup overview for laser ablation loading. The ablation laser enters through the top viewport of the vacuum chamber. (b) Neutral barium atomic energy structure, including the 2-step photoionization process to produce barium ions described in Section 3.1.1. These figures were generated by my colleague Brendan M. White for the purposes of being published in [48] and are included here for reference.

options, with ablation loading being on the order of seconds whereas oven-loading takes on the order of minutes [48].

Ablation loading does present, however, its own unique set of challenges [48]. There exists a high variance between the neutral atom flux from one ablation pulse to the next [48]. Furthermore, there exists a spatial variance across the $BaCl_2$ target introduced by both imperfections in the material and the geometry of the experiment, including the angle of the alignment of the ablation laser relative to different points on the target surface [48]. The source of this variance is what motivated our investigation into better characterizing the ablation process so as optimize the reproducibility of the loading process [48]. The results of this investigation are presented in this chapter.

## 3.2 Conditioning Characterization

We found that an important step in reliably loading barium ions into the trap consisted of what we defined as pre-*conditioning* the ablation spots on the $BaCl_2$ target [48]. *Conditioning*, in this context, is defined as ablating fresh spots on the $BaCl_2$ target with a series of higher fluence ablation pulses to essentially activate or improve the neutral atom flux from said spot at lower pulse fluences [48].

The goal was to characterize both the spatial and temporal variation of the atomic flux across the $BaCl_2$ target as a result of conditioning, with the ultimate goal of establishing a protocol for trapping ions consistently using laser ablation loading [48].

### 3.2.1 Conditioning Experiment Overview

All of the data collected in this section was from a high-volume, natural-abundance 30 mg $BaCl_2$ salt target [48]. Each spot on the target was selected using a previously calibrated x-y coordinate grid system and the ablation laser was aligned to each spot using two servo motors on mirror mounts [48]. The laser frequencies were set to be on resonance with the $^{138}Ba^+$ isotope for the purposes of these experiments since it is the most abundant of the barium isotopes, and thus also the easiest isotope to load into the trap [48].

Ion-flux fluorescence counts were collected by irradiating the ions with a combination of 493 nm light for Doppler cooling, and 650 nm light to repump out of the unwanted $D_{3/2}$ state (see Figure 4.1) [48]. Geometrically, both of these lasers are co-propagating with the 554 nm beam [48]. The photons produced as a result of both neutral and ion-flux fluorescence were collected by an imaging objective and read out using a photomultiplier tube (PMT) [48]. The collected fluorescence corresponds to the number of PMT counts collected with a 55 $\mu$s integration time, starting 145 $\mu$s after an ablation pulse hits the $BaCl_2$ target [48].

The lifetime of a fresh spot on the $BaCl_2$ target was determined to be approximately $10^4$ pulses, and approximately $2x10^3$ after reconditioning [48]. For this reason, a total of $10^3$ pulses were collected from each fresh spot for each conditioning experiment so as not to diminish the lifetime of each of these spots significantly for future use (see Figure 3.3).

The regions of high-fluence versus low-fluence were determined by collecting fluorescence counts over a range of different fluence values (see Figure 3.2). The conditioning fluence regime was established to be anywhere above 0.3 J/cm$^2$ [48]. Observable neutral atom fluorescence occurs for fluences anywhere above 0.1 J/cm$^2$, while observable ion fluorescence occurs above 0.25 J/cm$^2$ [48]. The best spots to use on the target correspond to the ones where the production of a neutral atom flux is not accompanied by any incoming ion flux [48]. An influx of ablated ions results in an undesirable excess charge build-up on the trap electrodes, thus making trapping longer chains of ions more challenging [48]. For these reasons, a conditioning fluence of 0.48 J/cm$^2$ was selected for the conditioning characterization experiments, with a corresponding low-fluence pulse of 0.2 J/cm$^2$, a low-fluence value which is still well below the ion-regime in Figure 3.2 [48].

More specifically, these experiments consisted of alternately exposing each fresh spot on the $BaCl_2$ target to 10 conditioning pulses followed by 10 low-fluence pulses and so forth, for a total of $10^3$ pulses per spot [48].

### 3.2.2 Conditioning Experiment Results

#### Observations

Each data point in Figure 3.3 is the average over a series of 10 pulses collected for each of the low and corresponding high-pulse energy counts to account for statistical variability across the neutral fluorescence produced by each ablation pulse [48]. The error bars displayed for each point consist of the standard deviation across those 10 pulses [48].

Although the outcome from conditioning was highly variable, some common behaviours were observed [48]. From all of the spots collected across the $BaCl_2$ target, 3 common behaviours were observed [48]. After conditioning, a spot could either be classified as a low ($<$ 10 counts, typically near background), moderate (10-50 counts) or high-yield spot ($>$ 50 counts), depending on the range of neutral fluorescence counts each spot asymptotically reaches. We also observed that this asymptotic behaviour occurs after approximately 200 pulses (see Figures 3.3, 3.4 and 3.5).

Spots that are in the central band of the target are more likely to produce moderate to high-yield spots (desired) than those around the perimeter of the target (Figures 3.4 and 3.5). Furthermore, spots that are located along the perimeter of the target did not produce any high-yield spots, producing nearly a 50/50 split between moderate and low-yield spots (see Figure 3.5). However, it should be noted that regardless of the location of the ablation laser relative to the $BaCl_2$ target, conditioning does not always work for every single new spot [48].

Seventeen fresh spots were collected near the target centre to further investigate these 3 common behavioural patterns, fifteen of which are represented in Figure 3.4, the majority of which were observed to be low-yield spots [48]. 5/17 fresh spots emerged as high-yield, 4/17 emerged as moderate-yield and 8/17, nearly half of the spots collected in the central region, emerged as low-yield [48].

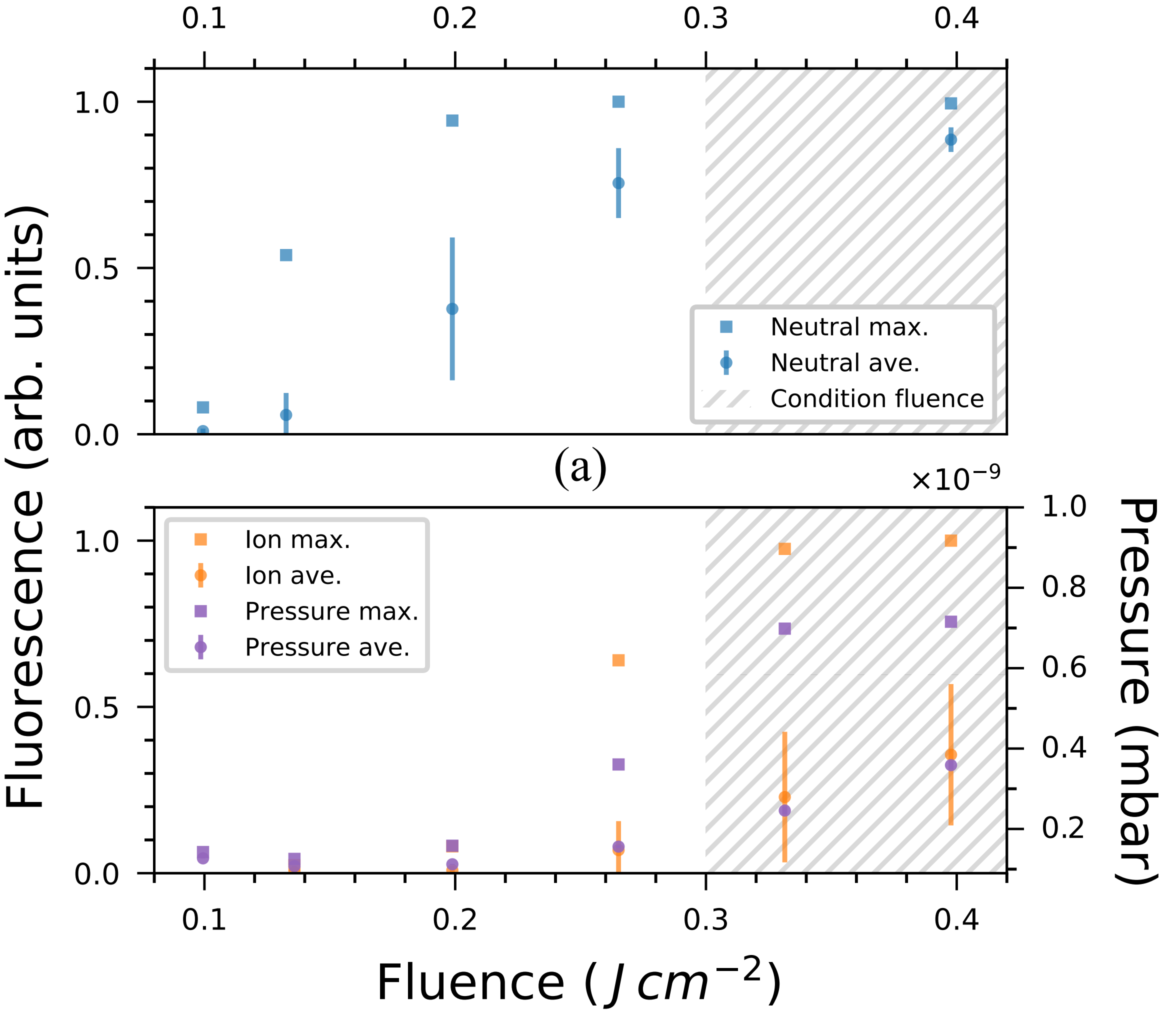

(a)

(b)

Figure 3.2: Neutral atom fluorescence (a) vs. ion fluorescence (b) regions as a function of fluence values [48]. This figure was generated by my colleague Brendan M. White for the purposes of publication in [48] and is included here for completeness.

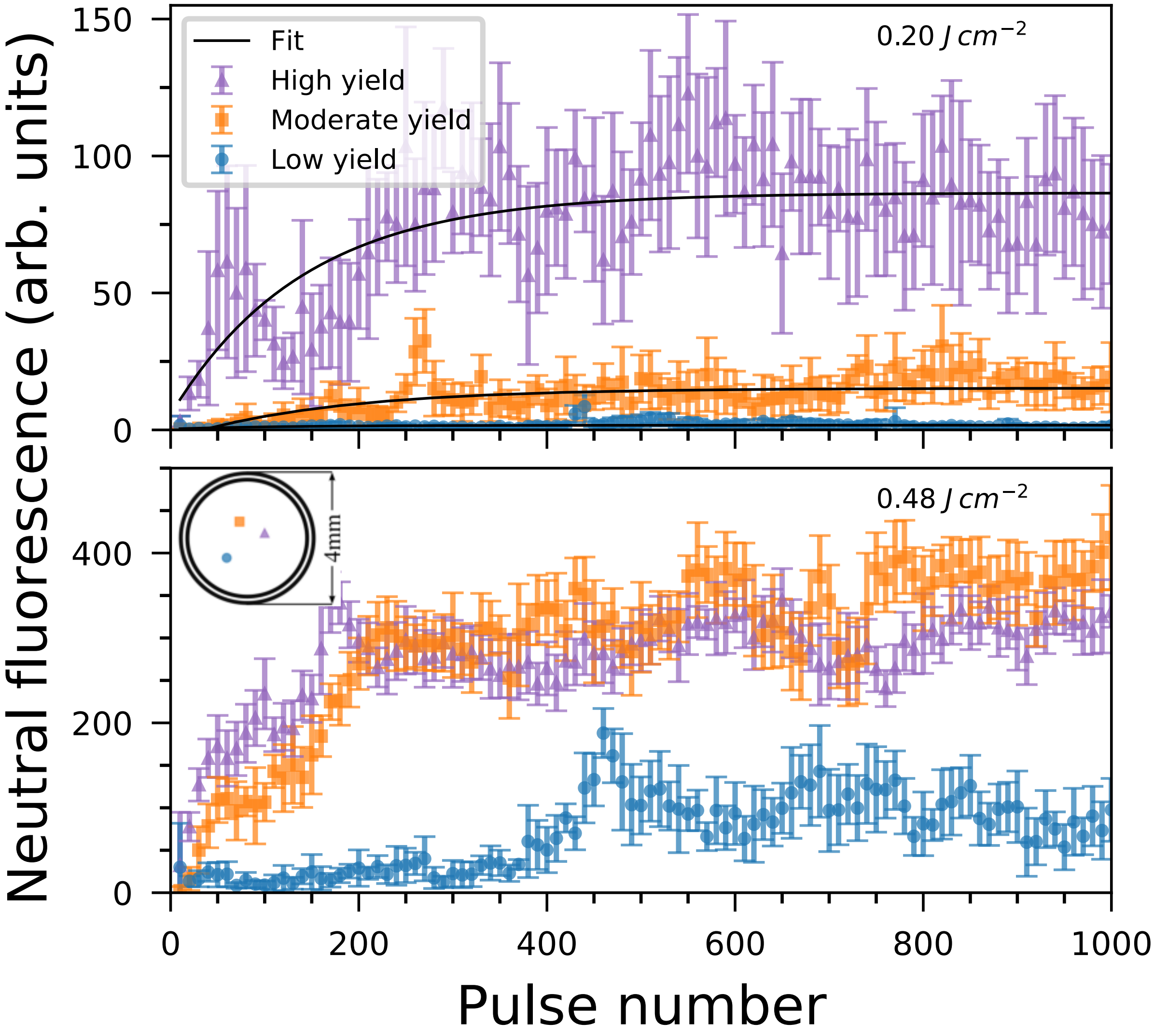

Figure 3.3: The top plot consists of neutral fluorescence counts collected at low-pulse energy (0.20 J/cm$^2$), whereas the bottom plot consists of the corresponding conditioning counts collected at high (conditioning) pulse energy (0.48 J/cm$^2$). This figure showcases the three most common behaviours found amongst the spots on the target, as discussed in Section 3.2.2. The colours of each spot displayed on the inset target map coordinate with the colours of each of the data sets represented in the plots. This figure was also generated by me and my colleague for the purposes of publication in [48].

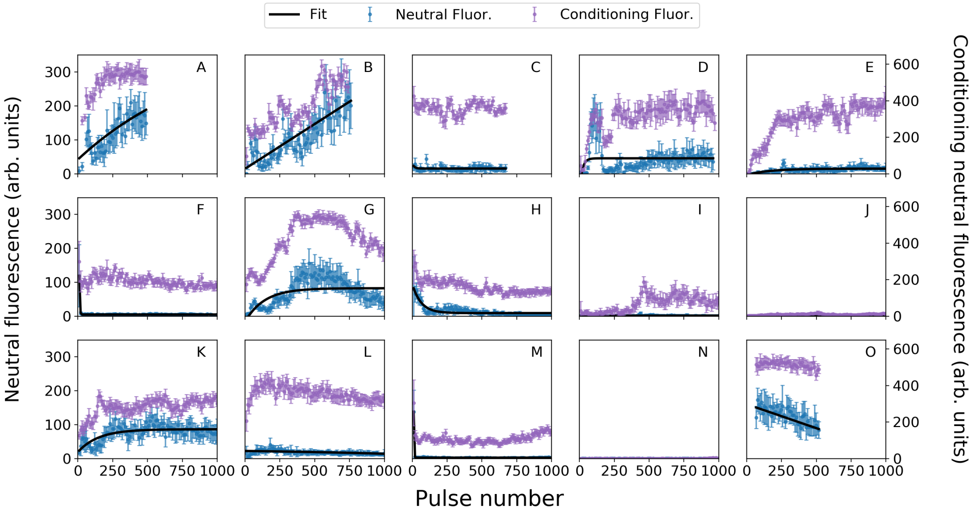

Figure 3.4: This figure is an overview of the conditioning spots collected from the **central** band of the target (see Figure 3.5 for a target map). Spots A, B, G, K and O are high-yield, spots C, D, E and L are moderate-yield and spots F, H, I, J, M and N are low-yield spots, as discussed in section 3.2.2.

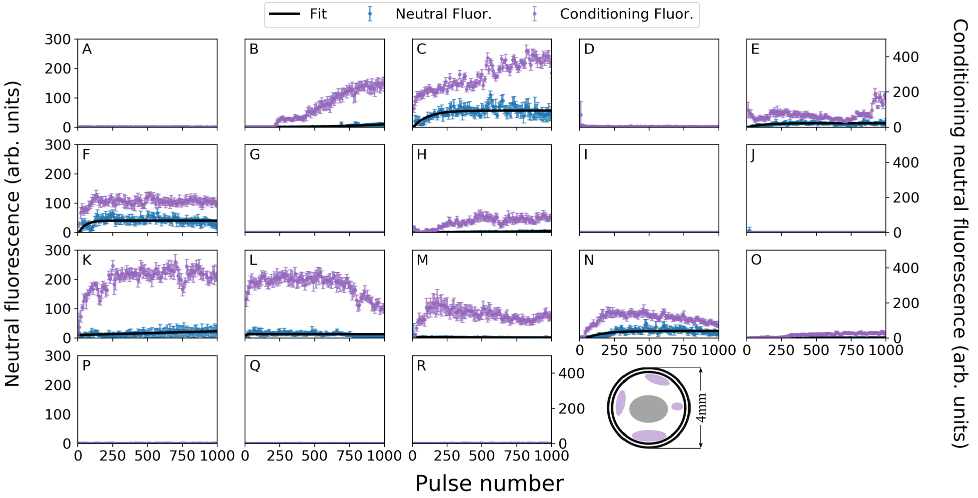

Figure 3.5: This figure is an overview of the conditioning spots collected from around the **perimeter** of the target (see inset target map). Spots spots B, C, E, F, K, L and N are moderate-yield while the majority of spots (A, D, G, H, I, J, M O, P, Q, R) are all low-yield spots, with no high-yield spots found in this subset [48].

### 3.2.3 Hypotheses on Characterization Behaviour

We hypothesize that the higher-fluence, or *conditioning* pulses, have a plasma cleaning effect on the $BaCl_2$ target surface, thus yielding better neutral fluorescence counts when returning to a lower pulse fluence [48]. By this theory, the conditioning pulses work by removing surface contaminants from the target at a given spot, thus transforming the surface shape at that spot and subsequently improving the angle of the ablation beam relative to the surface [48].

With regards to the spatially variability of the fluorescence across the target, we hypothesise that the central region is more likely to produce higher yield spots for two reasons related to the experiment infrastructure and relative geometry [48]. Firstly, the spots located on the left and rightmost edges of the target may be impacted by a Doppler shift caused by the ablation plume not being orthogonal to the 554 nm beam path [48]. Secondly, the top and bottom edges of the target, may be obstructed by one of the trap rods [48].

### 3.2.4 Algorithm for Assessing a New Spot

From the results of the conditioning experiments discussed in this chapter, determining the viability of a fresh spot on the $BaCl_2$ target can be summarized in the following set of steps [48]:

1. Start by checking for neutral fluorescence at low-pulse energy to see if the spot is already moderate to high-yield without any additional conditioning necessary. If the spot is, however, low to moderate yield after $\sim 10$ low-fluence pulses, proceed to Step 2.
2. By referring to the running record of spots we have used, locate a fresh spot on the $BaCl_2$ target, preferably in the central region of the target if possible.
3. Move the ablation laser beam pointing to the chosen spot.
4. Alternatively ablate the chosen spot with 10 conditioning pulses, followed by 10 low-fluence pulses, for a total of 200 conditioning pulses to determine whether it consists of a low, moderate of high-yield spot. This process takes on the order of minutes.
5. If the spot is moderate to high-yield ($>30$ low-fluence neutral fluorescence counts), this should be sufficient to conduct ion-trapping experiments with.

6. Alternatively, if the spot is low-yield, move to another spot approximately 1 beam-waist away.

Empirically, as discussed in section 3.2.2, this process should work approximately 30 % of the time, meaning approximately 1/3 spots should yield a functional spot on the target [48]. Furthermore, with this technique, we were able to achieve a loading selectivity of 32±5 % with our $^{137}\mathrm{Ba}^{+}$ ions, significantly higher than its natural abundance of 11.2 %.

# Chapter 4

# $^{137}$Ba$^{+}$ Qubits: Experiment Infrastructure

In Chapter 3, I discussed the infrastructure that has already been developed and tested to reliably trap and cool various isotopes of Ba$^{+}$. Once they are successfully trapped, the next step towards being able to use this platform for an entangling gate operation is thus to implement the necessary frameworks to be able to use these ions as qubits.

The focus of this chapter is therefore to give an overview of the experimental plans to build-up the required systems and functionality in the laboratory to be able to use $^{137}$Ba$^{+}$, one of two isotopes in our proposed dual-isotope entangling schemes (see Chapter 2.2) as a qubit. It will also include details on the infrastructure that has been put in place thus far, with a specific focus on the systems I have worked on. Longer-term, the goal is to eventually expand to using $^{137}$Ba$^{+}$ as qu**d**its, however this discussion is beyond the scope of this thesis [29, 28].

More specifically, this chapter will examine the steps taken towards developing the necessary infrastructure towards performing functional state preparation and measurement (SPAM) on $^{137}$Ba$^{+}$ qubits and with $^{138}$Ba$^{+}$ qubits, our naturally most abundant isotope. This is a necessary milestone in the life-cycle of a dual-isotope entangling gate infrastructure [22].

Note that in the text, all of the wavelengths quoted in this chapter will be rounded to the nearest integer value for a specified transition. In Figure 4.1, they are rounded to the nearest decimal.

## 4.1 Experiment Overview

This section will give an overview of the infrastructure necessary to be able to use $^{137}$Ba$^{+}$ as qubits in practice. These bring-up plans were first developed by a former post-doctoral researcher in our lab, Dr. Matthew Day [1], based on [10] and further refined through discussions with the entire research group, as well as through implementation in the laboratory.

### 4.1.1 $^{137}$Ba Energy Structure

To begin, it is important to visualize the energy structure of all of the different states we are trying to address with the infrastructure detailed in this chapter. Figure 4.1 will provide a reference for mapping the relevant transitions discussed in this chapter onto an energy level diagram of barium.

### 4.1.2 Experiment Modules

The sequence of operations necessary to successfully use $^{137}$Ba as a qubit are, in order:

1. Isotope-selective Loading (see Chapter 3)
2. Doppler Cooling: effective cooling is necessary to maintain ion coherence and improve the duty cycle of experiments.
3. State Preparation (SP): necessary to know which qubit state the ion is starting in, which in turn affects the subsequent states it has access to according to atomic transition rules (see [4]. Also necessary for item 4, Measurement.
4. Shelving/Measurement (M): allows us to measure which qubit (atomic) state the ion ended up in. Measurement also requires a ‘Repump’ operation in our case to prevent the slowdown of the SPAM duty-cycle.

Each of these steps corresponds to these respective subsystems:

1. 554 nm & 405 nm laser subsystems
2. 493 nm cooling & 650nm laser subsystems

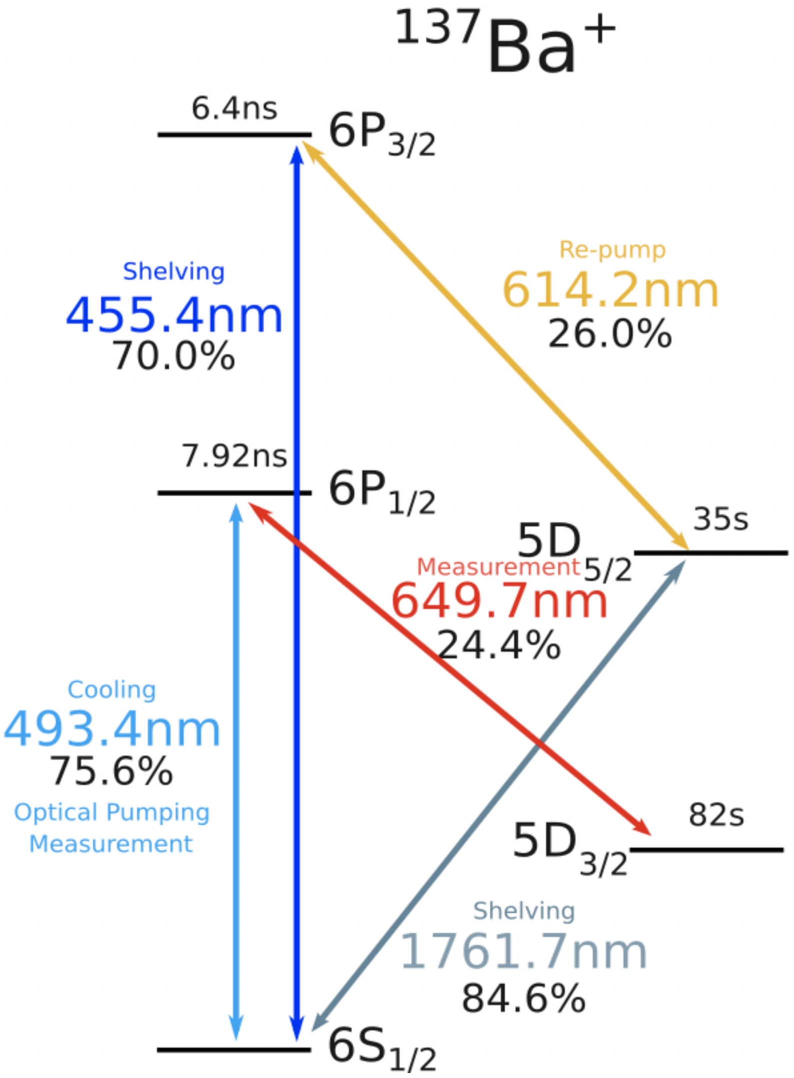

Figure 4.1: Energy level diagram of $^{137}Ba^{+}$, including captions of what each of the transitions are used for. Wavelengths are rounded to the nearest decimal point. Also includes the lifetimes of each of the energy levels. The % value indicates the probability of that transition occurring. Adapted from [4].

3. 493 nm optical pumping laser subsystem
4. 455 nm / 1762 nm laser subsystem for shelving and a 614 nm repump laser subsystem

Each subsystem will be discussed in further detail with how it pertains to $^{137}Ba^+$ as a qubit with a specific focus on items 3 and 4 (SPAM).

### Isotope-Selective Loading

In Chapter 3, a method to reliably load $^{137}Ba$ ions into the trap was presented in detail. However, once the ions are trapped, we want to be able to address this isotope to be able to perform the necessary qubit operations with it. These operations will be discussed in further detail in the subsequent sections.

### Doppler Cooling

The $6S_{1/2} \leftrightarrow 6P_{1/2}$ optical transition (see Figure 4.1) is used for Doppler cooling the ion. This transition is on resonance with our 493 nm-wavelength Toptica laser, which has a power output of 10-20 mW [4]. By detuning the 493 nm laser on the order of MHz from this transition and collecting the resulting fluorescence as counts on our PMT, we can verify if the fluoresence rates (counts) are stable, implying that the ions have cooled. This technique has already previously been implemented to cool $^{138}Ba$ ions in our trap and therefore only requires a modification at the scripting level to be automated for $^{137}Ba^+$ [4, 28]. As per Figure 4.1, the $6P_{1/2}$ state has an approximate 25 % probability of decaying into the long-lived $5D_{3/2}$ state (state with a lifetime of 82 s), and thus must be re-pumped back into the $6P_{1/2}$ state using a 650 nm re-pump laser [4]. Any state on the order of seconds would significantly decrease the duty-cycle of the qubit operations, thus harming the computing speed of the TIQI processor. The 650 nm beam-path had previously been implemented to address $^{138}Ba^+$ [4] and its functionality is therefore already in place and ready to be used for $^{137}Ba^+$ qubits.

Further verification that the ions have in fact been cooled to the Doppler limit will be discussed in the subsequent **Shelving** subsection.

### State Preparation

State preparation involves preparing $^{137}Ba^+$ in the $\left|S_{1/2}, F = 2, m_F = 0\right\rangle$ state. This process involves transferring the population from the $\left|S_{1/2}, F = 2, m_F = +2\right\rangle$ to the

$\left|S_{1/2}, F=2, m_F=0\right\rangle$ state, since the $|m=0\rangle$ state is less sensitive to magnetic field fluctuations.

In order to first reach the $\left|S_{1/2}, F=2, m_F=+2\right\rangle$ state, the optical pumping beam (493 nm laser) must be used to pump into this maximum angular momentum state for the $\left|S_{1/2}\right\rangle$ manifold. The 493 nm beam path must be circularly polarized in order to be able to use it to transfer populations from $|m\rangle$ to $|m+1\rangle$ hyperfine states. The 650 nm re-pump must also be on during the optical pumping process as well, to re-pump out of the long-lived $\left|D_{3/2}\right\rangle$ state.

### Shelving

Shelving the $^{137}\text{Ba}^{+}$ population consists of introducing a 1762 nm wavelength beam to pump the unused $\left|S_{1/2}\right\rangle$ qubit states into the $\left|D_{5/2}\right\rangle$ manifold [4, 10]. The $\left|D_{5/2}\right\rangle$ state serves as a good candidate for shelving due to its long lifetime of ∼30 s. By shelving these qubit states, they become insensitive the 493 nm and 650 nm fluoresence lasers, thus producing zero fluoresence, colloquially known as the ion "going dark" [4]. Further work has been done to explore which levels in the $D_{5/2}$ manifold to shelve to, however this work is beyond the scope of this thesis and I will refer you to [4].

In order to perform the state preparation discussed above, we originally planned on using a home-built 455 nm laser (see section 4.2.2) to shelve ion populations into the $\left|D_{5/2}\right\rangle$ state. For that approach, it is necessary to be able to distinguish between the fluorescence counts from the $\left|S_{1/2}, F=1\right\rangle$ and $\left|S_{1/2}, F=2\right\rangle$ states, since the population transfer occurs via the $\left|S_{1/2}, F=1\right\rangle$ state. In order to achieve this, microwave pulses at varying frequencies can be applied to search for the population transfer to the $\left|S_{1/2}, F=1, m_F=+1\right\rangle$ state. The same sweep can then be done to transfer to the $\left|S_{1/2}, F=1, m_F=0\right\rangle$ state starting from the $\left|S_{1/2}, F=1, m_F=+1\right\rangle$ state. The shelving experiment involves pumping all of the $\left|S_{1/2}, F=2\right\rangle$ population into the the metastable $\left|D_{5/2}\right\rangle$ state by applying a long enough 455 nm shelving pulse while searching for the microwave frequency to transition to $\left|S_{1/2}, F=1, m_F=+1\right\rangle$. This would be done following an optical pumping sequence. By measuring the resulting population of the $\left|S_{1/2}\right\rangle$ state would thus provide a measurement of the $\left|S_{1/2}, F=1\right\rangle$ state with all of the $\left|S_{1/2}, F=2\right\rangle$ states shelved.

However, in practice, we decided to go in a different direction, without the 455 nm laser (see section 4.2.2 for further detail as to why we didn't pursue this design). We instead acquired a narrow linewidth Toptica 1762 nm laser for our shelving and measurement procedure since it was more readily available to us and thus decided our qubit encoding and furthermore, how we would be performing our measurement protocol.

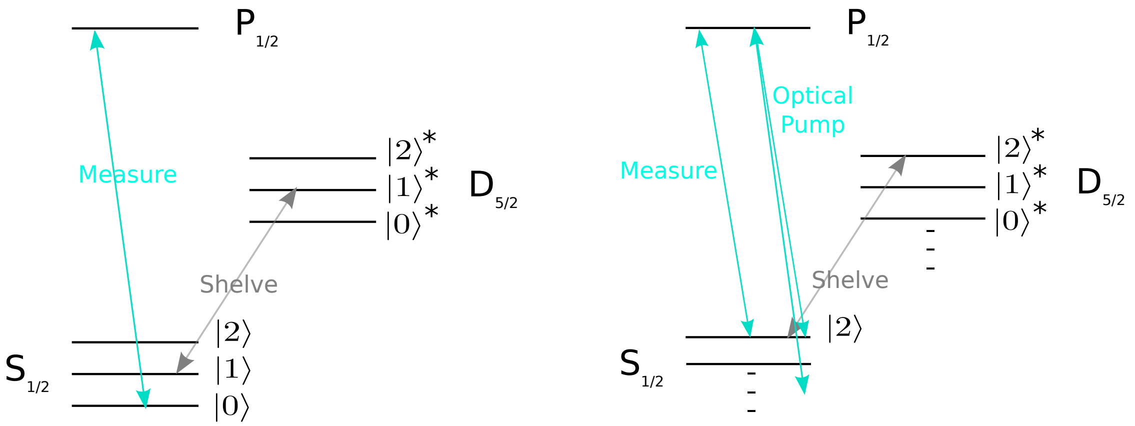

(a) (b)

Figure 4.2: (a) Previous encoding proposal in the $\left|S_{1/2}\right\rangle$ manifold. The asterisks * correspond to the shelved equivalents of the $\left|S_{1/2}\right\rangle$ qu**d**it states $|0,1,2\rangle$. The pulse sequence associated with this involves shelving the qudit states to the $\left|D_{5/2}\right\rangle$ state, followed by a fluorescence measurement on the $S_{1/2} \leftrightarrow P_{1/2}$ transition, de-shelving with a second 1762 nm pulse and repeating the cycle with a new state. (b) The new sequence involved optical pumping into the stretch state of the ground state manifold, $\left|S_{1/2}, F=2, m_F=2\right\rangle$ as our state initialization step. The shelving/de-shelving, fluorescence steps are the same, however the relevant qu**d**its state will be encoded in the $\left|D_{5/2}\right\rangle$ manifold instead. Adapted from [4] and our conference poster presentation at DAMOP.

Thus now instead of encoding the qubit (or longer term, qu**d**it) states in the hyperfine states of $S_1/2$ manifold ie. the associated $m_F$ states to $\left|S_{1/2}, F=1\right\rangle$ and $\left|S_{1/2}, F=2\right\rangle$, we are encoding them in the $\left|D_{5/2}\right\rangle$ manifold [4]. More specifically, our approach had qubit states, $|q\rangle \equiv \left|S_{1/2}, F=1, m_F q\right\rangle$, where $q \in \{0,1,2\}$ with corresponding values of $m_F q \in \{-1,1,1\}$ [4]. With the current encoding procedure, we will still be optically pumping into the stretch state of the $S_{1/2}$ manifold, however, the $D_{5/2}$ manifold will now host the qubit states (see Figure 4.2).

### Qubit Measurement

The final step is then to measure all of the different qubit states by collecting state-dependent fluorescence measurements with the PMT. The qubit state determines whether the ion appears bright (fluoresces) or dark (no recorded fluorescence counts on the PMT or counts consistent with background) depending on which qubit state has/has not been shelved [10].

## 4.2 Corresponding Optics

This section will focus on the optics I worked firsthand on implementing to get the infrastructure described in Section 4.1 ready for experiments.

### 4.2.1 617nm Re-pump LED

This section discusses the work done to initially test our 617 nm LED to see if this method would be sufficient for re-pumping out of the $D_{5/2}$ manifold [20].

#### Scattering Rate

One of the primary considerations when looking at using a 617 nm diode for re-pumping over a 614 nm laser with an EOM is the scattering rate. The scattering rate of the transition affects the re-pump time, which in turn impacts the duty cycle of the experiment. As discussed in Chapter 1, speed is a very important metric in evaluating the feasibility of any computing platform. This section will focus on the theoretical scattering rate determined for the 617 nm LED and why we chose to go ahead with integrating it into the $^{137}\mathrm{Ba}^+$ infrastructure.

The idea to use an LED instead of a diode laser was implemented by Professor Chris Monroe's group at the University of Maryland to also re-pump out of the barium D5/2 state [20]. Their measured de-shelving time is ∼30 ms [20].

From Foot's text on atomic physics, the scattering rate from an arbitrary state is given by:

$$R_{scatt} = \gamma \rho_{22}, \tag{4.1}$$

where $\rho_{22}$ is the population of the excited state, in this case the $P_{3/2}$ state, and:

$$\gamma = 1/\tau \tag{4.2}$$

where $\tau$ is the lifetime of the state, which in this case is 6.4 ns (see Figure 4.1), the lifetime of the $P_{3/2}$ state.

From Foot Equation 9.4, the scattering rate can also be written as a function of the intensity of your laser (LED), $I = \frac{Power}{Area}$, and the detuning of said laser (LED) from the transition frequency, $\delta$ [13]:

$$R_{scattering}(I, \delta) = \frac{\gamma}{2} \frac{I/I_{sat}}{1 + I/I_{sat} + 4\delta^2/\gamma^2} \tag{4.3}$$

where $\delta = (\omega - \omega_0)$, with $\omega_0$ being the $D_{5/2} \leftrightarrow P_{3/2}$ transition frequency. In this case:

$$\omega_0 = 2\pi f_0 = 2\pi c/\lambda_0 \tag{4.4}$$

where $\lambda_0$ =614 nm, is the wavelength of the $D_{5/2} \leftrightarrow P_{3/2}$ transition.

From Foot Equation 7.85, the saturation intensity, $I_{sat}$, is [13]:

$$I(\omega_0) = I_{sat} = \frac{\pi}{3} \frac{hc}{\lambda^3 \tau} \tag{4.5}$$

where $\lambda$ in this case is the central wavelength of the diode, 617 nm.

By coupling as much of the 617 nm diode light possible into a multi-mode fibre, I measured the beam waist of the 617 nm diode at the fibre output to be ~1 mm in diameter, with a total output power of 1.7 mW. With these parameters, the total repump time, $1/R_{scatt}(I, \delta)$, is calculated to be ~97 ms, which is $<$ 35 s lifetime of the $D_{5/2}$ state, by summing over all of the detuning values, $\delta$. In this context, summing over all of the detunings refers to normalizing the intensity since the intensity data set provided by Thorlabs consists of a relative scale. This was achieved by summing over all of the intensity values in the 617 nm Thorlabs LED data (M617L4) set and then dividing our total intensity by this value to get a scale factor as such:

$$\text{scaleFactor} = \frac{I_{\text{total}}}{\sum \text{ThorlabsDataset}} \tag{4.6}$$

I then scaled the data set by this calculated scaleFactor as so:

$$\text{scaledI} = \text{ThorlabsDataset} \times \text{scaleFactor} \tag{4.7}$$

The area of the beam was assumed to be 1mm$^2$ for the purposes of these calculations (see Figure 4.3).

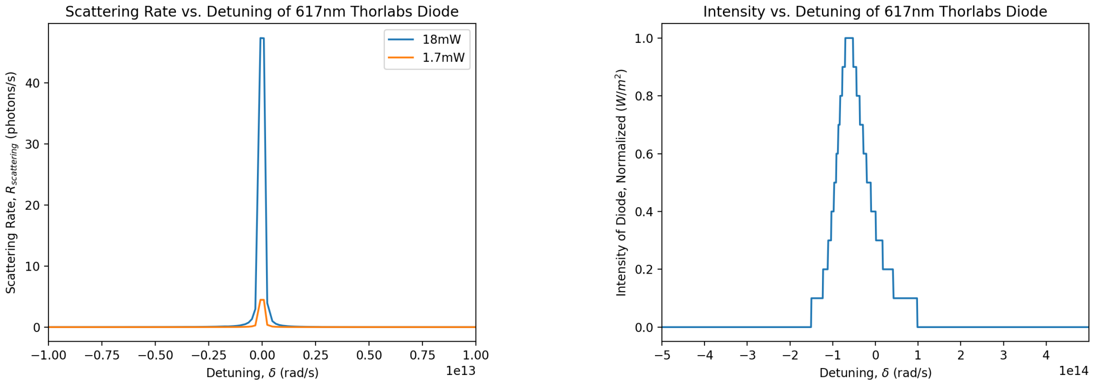

(a)

(b)

Figure 4.3: (a) Comparison of the scattering rates for different intensity values. The output powers are 18 mW and 1.7 mW, however the area used to calculate both rates are approximated as 1 mm$^2$ (b) This is the Thorlabs provided data-set for the 617 nm LED diode of normalized intensity vs. wavelengths, modified to be as a function of detuning from the 614 nm transition instead.

### Experimentally

However, my colleague, Pei Jiang Low, was able to improve the power output to 18 mW by using a Thorlabs direct fibre 617 nm LED. Again assuming an area of 1 mm$^2$ for the intensity values, this improves the theoretical repump time to ∼9 ms, which is well within our target repump range. This could further be improved by reducing the beam-waist of the LED.

The repump time with the LED was measured to be 1 s without the beam focused optimally (the beam was difficult to collimate). By re-pumping for 1 s my colleague was able to measure the ion going dark by applying a 1762 nm pulse 28/29 attempts, which is equivalent to 96.55 % of the time. The same experiment was run with a 617 nm LED repump time of 100 ms, which resulted in repumping only 21.05% of the time. The repump time with the 614 nm diode laser is on the order of $10^2$ $\mu$s, much quicker than what we could potentially achieve with the LED, thus motivating this approach. My colleague predicted that by pushing on optimizing the 617 nm LED beam path by better focusing the beam at the ions, the best we could improve the repump time to be is $\sim 200$ ms $< 10^2$ $\mu$s.

The beam waist was also a lot larger experimentally, was estimated to be approximately 4 mm. By simulating the above scattering rate with this diameter, the repump times are then calculated to be 146 ms and 1.55 s, for the 1.7 mW and 18 mW power outputs, respectively. This is more on the order with what we were observing on the lab (on the order of seconds). In practice, the beam was also clipped a lot due to the lack of efficient collimation. This would also result in some of the power being lost, so our power estimates in the simulation may not be accurate either. In summary, for a combination of all of these predictions and reasons, we decided to move forward with the 614 nm diode laser instead.

### 4.2.2 455nm Shelving Laser

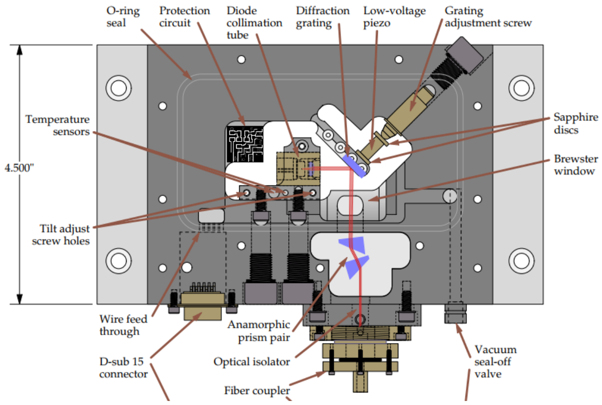

Figure 4.4: Original design by the Steck group at the Uinversity of Oregon [8]. Image from [48]. This was the design that was built by one of the former undergraduate co-op students for our experiment. The fibre-coupling and alignment was performed by me.

The initial goal with the shelving laser was to aid in the state preparation as described in section 4.1.2 by making use of the broader $S_{1/2} \leftrightarrow P_{3/2}$ linewidth transition. However, after several iterations, it was concluded that the vertical angle of the diffracton grating moves in conjunction with the horizontal angle, making it very challenging to align the laser optimally (see Figure 4.4). Therefore, we decided not to move forward with using this laser to perform further alignment for TIQI experimental purposes. We just wanted to note this design flaw in case this design ends up being used for future iterations of home-built lasers [8].

### 4.2.3 493nm Optical Pumping Laser

The 493 nm laser used for optical pumping (see Figure 4.1) is from Toptica as well, with an output power of 10-20 mW [4]. Its primary functions are for cooling, optically pumping into the stretch state, defined as the maximum angular momentum state, as well as for fluorescence measurements, as per section 4.1. We use a beam-splitter to split the beam into optical pumping and fluoresence/cooling beam paths and an acousto-optic modulator (AOM) to toggle each of these paths [4].

#### Producing Circularly Polarized Light

As discussed in section 4.1.2, producing a circularly polarized optical pumping beam is necessary to be able to be able to transfer populations into our desired hyperfine state. Producing circularly polarized light with the 493 nm optical pumping beam involves the following set of steps:

1. Insert a linear polarizer in the 493 nm optical pumping beam path. We use a Glan-Thompson polarizer.
2. This is followed by placing a second linear polarizer in the beam path after the first. This polarizer is known as the analyzing polarizer and is temporary to the overall setup.
3. A power meter is setup after both polarizers to measure the power fluctuations as we adjust the optics.
4. The second linear polarizer is rotated until it is oriented $\pi/2$ relative to the first polarizer. This is achieved when the power reading is a minimum since linearly polarized light will not pass through a polarizer oriented $\pi/2$ relative to its polarization. In other words, no component of the light's polarization is along the second polarizer's axis.
5. The quarter waveplate (QWP) is then inserted between both linear polarizers and rotated until a maximum power reading is achieved. This power reading should be half of the total initial power reading.
6. The analyzing polarizer is rotated to check if the power reading remains constant throughout the rotation.

## Theory

Following the derivation in [2], we can derive how this series of optics produces circularly polarized light.

Defining the angle between the transmission axis of the Glan-Thompson polarizer and the QWP as $\alpha$ and the electric field of the incoming 493 nm light as $E_{in} = E_0 \text{exp}(i\omega t)$, then the output of the electric field from the QWP is as follows along the axes of the QWP, $x'$ and $y'$:

$$\begin{cases} E_{x'} = E_0 \text{exp}(i\omega t + i\pi/2)\text{cos}(\alpha) \\ E_{y'} = -E_0 \text{exp}(i\omega t)\text{sin}(\alpha) \end{cases} \tag{4.8}$$

The QWP works by shifting the phase of the light along one of the axes by a quarter of a wavelength, or $\pi/2$. By defining the $x'$ axis as the slow axis, or axis that results in the light being slowed down by a quarter of a wavelength, the component of the electromagnetic field along the $x'$ axis includes a factor of $\text{exp}(i\pi/2)$.

Subsequently defining the angle between the second analyzing polarizer and the transmission axis of the first linear polarizer as $\beta$, the angle between the QWP slow axis of propagation and the second analyzing polarizer is then $(\beta - \alpha)$. Following a similar projection onto the transmission axes of the analyzing polarizer and adding up the components along both axes, the electromagnetic field exiting the analyzing polarizer is then:

$$E_{out} = -E_0 \text{exp}(i\omega t)[\text{exp}(i\pi/2)\text{cos}(\alpha)\text{cos}(\beta - \alpha) - \text{sin}(\alpha)\text{sin}(\beta - \alpha)] \tag{4.9}$$

The measured power is proportional to the output intensity of the beam. The intensity is proportional to the electromagnetic field amplitude as follows: $I \propto |E|^2$, where:

$$|E|^2 = E_0^2[\text{cos}^2(\alpha)\text{cos}^2(\beta - \alpha) + \text{sin}^2(\alpha)\text{sin}^2(\beta - \alpha)] \tag{4.10}$$

Since in our setup we aligned the analyzing polarizer to be $\pi/2$ relative the first linear polarizer, therefore $\beta = \pi/2$ in all of the above equations.

By taking the derivative of the intensity, $I$, and solving for the maximum, we see that the maximum occurs when $\alpha = \pi/4$. By including these values for $\alpha$ and $\beta$ into the equation for $I$, we see that the intensity after the QWP is $I = I_0/2$. Thus, the power at the output is also halved, as per Step 5 above.

### Elliptical Polarization Compensation

During alignment, there was some ellipticity that was observed in the beam path when the polarization was measured with an analyzing linear polarizer after the trap. It was concluded that the mirrors used to redirect and focus the 493 nm light into the trap do introduce some ellipticity error due to their reflecting S and P polarizations of light at slightly different reflectance % values for 493 nm wavelength light. However, the aberration is minimal, thus we have decided to proceed without any ellipticity compensation at this time, with future plans in place to introduce correcting optics into the beam path if need be to improve the purity of circular polarization for our experiments in the future.

### Outlook

Since the time of the writing of this thesis, our research team has fully accomplished our goals of successfully optically pumping, re-pumping and shelving as demonstrated to perform successful SPAM experiments with $^{138}\mathrm{Ba}^{+}$. We have since measured an optical pumping time $< 2\ \mu$ s. Furthermore, we were able to perform state transfers (shelving) from the $\left|S_{1/2}\right\rangle$ to $\left|D_{5/2}\right\rangle$ manifold with 99 % fidelity, by measuring the Rabi oscillations.

# Chapter 5

# Summary & Outlook

## 5.1 Summary

This thesis introduced the steps we have taken thus far towards implementing dual-isotope entangling gates with two different isotopes of barium, namely $^{137}\mathrm{Ba}^{+}$ and $^{133}\mathrm{Ba}^{+}$, with the ultimate goal of harnessing this architecture to develop new TIQI capabilities, such as MCMR and concurrent sympathetic cooling. This in turn would greatly benefit the scale of quantum algorithms we would be able to run successfully on these devices, which still presents a limitation in realizing the full potential of quantum systems.

At the time of writing of this thesis, we are actively working with multiple of the proposed transitions for qudit work, namely the $\left|S_{1/2}\right\rangle$ to $\left|D_{5/2}\right\rangle$ manifold, with both our naturally most abundant isotope, $^{138}\mathrm{Ba}^{+}$ and one of our other proposed qubits $^{137}\mathrm{Ba}^{+}$ [29]. This puts us in an excellent position to pursue immediate next steps in improving our SPAM fidelities by tuning the architectures discussed in Chapter 4, thus optimizing optical pumping and repump times. As per the product life-cycle of some of the most advanced trapped-ion quantum computing platforms, like the one being developed by Honeywell, SPAM fidelities are one the early milestones indicative of the feasibility of a proposed architecture [22, 37]. The rest of the functionality we proposed motivating this dual-species approach, such as harnessing sympathetic cooling and MCMR capabilities, will be built up from these early necessary markers [22].

Of course, even before SPAM can be performed on one of our $^{137}\mathrm{Ba}^{+}$ qubits, we must be able to reliably isotope-selectively load these ions into our trap, so that we may work with both of them. After extensive investigation of both the ablation-loading process and the ablation target from which we ablate and load our ions, we can now confidently load both $^{138}$Ba$^{+}$ and $^{137}$Ba$^{+}$ using this technique from our BaCl$_2$ target [48], the details of which were the focus of Chapter 3. In that chapter, I characterized the reliability of the ablation loading technique for our specific goals, along with the spatial and temporal variation of the atomic flux across the barium-salt target. We presented a protocol we coined 'conditioning' that allows us to prepare ablation spots on our salt target with higher ablation pulse fluences (0.48 Jcm$^{-2}$) to provide higher yields (neutral fluorescence counts) at lower pulse fluences (0.20 Jcm$^{-2}$). This protocol helps us to avoid flooding the trap with a plume of ions, which leads to unwanted charging over time [48]. In Chapter 3, I demonstrated a $^{137}$Ba$^{+}$ loading selectivity of 32±5%, a significant increase over the natural abundance of this isotope of 11.2% using this technique.

We also wanted to be able to understand how the motional mode structure of a dual $^{137}$Ba$^{+}$/$^{133}$Ba$^{+}$ chain would behave, especially relative to its single species ($^{133}$Ba$^{+}$ chains) and dual-species counterparts ($^{133}$Ba$^{+}$/$^{171}$Yb$^{+}$ chains). In Chapter 4, I discussed how the theoretical motivation for TIQI entangling gates relies on the motional modes acting as a bus for entangling the internal (or qubit) states of the ions. Furthermore, I discussed how the participation of each ion in the mode, as measured by their respective motional mode participation vector, $b_{im}$, is proportional to the rate of sympathetically cooling of the system, one of the capabilities we're aiming to harness by moving towards this dual-isotope architecture. Thus, calculating the motional mode structure for the novel dual-barium-isotope system we're proposing is a necessary first step in analyzing this new system, and the motional mode structures for an $N$ =3 ion-chain were presented in Figures 2.2, 2.3 and 2.4 by simulating the behaviour of these chains. Through this investigation, we were able to confidently conclude that these systems would much better present themselves for sympathetic cooling purposes relative to their dual-species counterparts; they have a relative larger motional mode participation across both isotopes while still retaining their MCMR capability, which single-species don't lend themselves to as well, as discussed and compared in Chapter 1. Thus, the motional mode structure of a dual-isotope chain won't be a limiting factor in the same way that two-species chains struggle with this mass difference as in [43].

## 5.2 Outlook

Since the writing of this thesis, our team has decided to proceed with working with $^{138}$Ba$^{+}$ instead of $^{133}$Ba$^{+}$ as our second isotopic species due to difficulties faced with loading from our low-volume radioactive BaCl$_2$ target. However, $^{133}$Ba$^{+}$ is a promising species, with many industrial TIQI quantum ventures now also pursuing this species for its many desirable qualities that also motivated our pursuits as per [29], such as its nuclear spin of $\frac{1}{2}$ and comparable coherence times. However, a PhD student on our open-access TIQI quantum computing project, QuantumIon, is actively investigating different target preparation techniques for this very reason, something we may be able to explore and further apply in QuditLab to extend the work. However, both of our $BaCl_2$ targets rest inside of our vacuum chamber for optimal loading geometry and thus replacing the radioactive target would require breaking vacuum, which does delay other concurrent experiments. $^{138}Ba^+$ serves as a great second species as well with an even closer mass to $^{137}Ba^+$ with the added benefit of ease of loading, since it is the most naturally abundant isotope of barium with a natural abundance of 71.7 %.

Furthermore, whereas with our current infrastructure we have now successfully been able to prepare and measure the qubit states of both $^{138}Ba^+$ and now with $^{137}Ba^+$ by performing Rabi experiments on the order of 10's of transitions from the $S_{1/2}$ to $D_{5/2}$ state, we have yet to co-trap both of these isotopes and perform SPAM or cooling protocols on either/both of them. We would want to investigate the experimental efficiency of our sympathetic cooling protocol by exploring how effectively we can cool $^{137}Ba^+$ ions by cooling $^{138}Ba^+$, for example, while still retaining the qubit information encoded in $^{137}Ba^+$ or performing SPAM with the other. It would be great if we could continuously cool one isotope while resetting the other's qubit state, since this would be the equivalent of a MCMR and improve the scale of algorithms that could be run on our device [14].

Nevertheless, we have also yet to perform any entangling gates with either of these isotopes, so that would be a necessary experimental milestone. Once our SPAM fidelities are optimal, it would be interesting to measure what our single-species entangling gate performance fidelities are as well. This bring-up life-cycle of a novel dual-isotope system, starting with designing and building infrastructure, theoretical calculations, followed by SPAM and single-species coherence operations are typical for an end goal such as moving towards dual-isotope entangling gates for TIQI platforms [43, 22].

From a theoretical standpoint, further investigation of the behaviour of a dual-barium-isotope system with $^{138}Ba^+$ can be conducted in parallel alongside the experimental bring-up plans. For example, one avenue to explore would be which modes and thus, which configurations, would lend themselves best to cooling protocols. In recent work done at U. Maryland [43], they found that the transverse modes are much harder to cool than the axial modes regardless of configuration for dual-species with larger mass differences, which is something we would want to investigate with our two isotopes. This would go hand in hand with co-trapping experimental plans, such as exploring if certain configurations are easier to load/cool than others based on geometric or alignment limitations. The simulations would feedback into the experimental work by helping us benchmark what we expect to see for a given ion-chain configuration.

Similar work has also been done to compare against pulse-shaping techniques such as amplitude and frequency-modulation for both transverse and axial modes [43]. Using a pulse-shaping technique to improve the performance of entangling gates has been implemented extensively in TIQI systems over the recent years and would be a longer term experimental goal for us. However, theoretically it would be interesting to investigate which configurations would lend themselves best for our purposes. Simulating longer chains of ions is always challenging since the number of modes does scale with the ion chain length, $N$. However, often the symmetry of the chain could be a marker of similar behaviours for longer chains. Information such as the required Rabi frequencies to achieve a target entangling gate fidelity could be pulled from such an investigation. $\Omega_{max,m}$ [43], the maximum Rabi frequency, is impacted by the participation in the mode $m$, thus modes where both ions participate more equally, $b_{im} \sim b_{j,m}$, are expected to perform better, although this is open to further theoretical investigation. Further building on this idea, which pair of ions would be best to entangle in a given chain and whether it would be possible to entangle any two is still open for further exploration as well. Each pair has a distinct pair of mode participation vectors that go along with them, thus each would require a more or less involved pulse-shaping scheme to achieve the same entangling gate performance, which would be an interesting path to further investigate.

# References

[1] Ba-137 qubit bringup. `https://ions-wiki.iqc.uwaterloo.ca/index.php?title=Ba-137_qubit_bringup`. Accessed: 2021-2022.

[2] Lab 8: Polarization of light. `https://www.yorku.ca/marko/PHYS2212/Lab8.pdf`. Accessed: January-February 2022.

[3] D. T. C. Allcock, W. C. Campbell, J. Chiaverini, I. L. Chuang, E. R. Hudson, I. D. Moore, A. Ransford, C. Roman, J. M. Sage, and D. J. Wineland. *omg* blueprint for trapped ion quantum computing with metastable states. 2021.

[4] Brendan Bramman. Measuring trapped ion qudits. Master's thesis, University of Waterloo, 2019.

[5] Kenneth R Brown, Jungsang Kim, and Christopher Monroe. Co-designing a scalable quantum computer with trapped atomic ions. *npj Quantum Information*, 2016.

[6] C.D. Bruzewicz, R. McConnell, J. Stuart, J.M. Sage, and J.Chiaverini. Dual-species, multi-qubit logic primitives for $Ca^+/Sr^+$ trapped-ion crystal. 2019.

[7] Colin D. Bruzewicz, John Chiaverini, Robert McConnell, and Jeremy M. Sage. Trapped-ion quantum computing: Progress and challenges. 2019.

[8] Eryn C. Cook, Paul J. Martin, Tobias L. Brown-Heft, Jeffrey C. Garman, and Daniel A. Steck. High passive-stability diode-laser design for use in atomic-physics experiments. 2012.

[9] C. Monroe D. Leibried, R. Blatt and D. Wineland. Quantum dynamics of single trapped ions. *Reviews of Modern Physics, 75(1):281-324*, 2003.

[10] M.R. Dietrich, N. Kurz, T. Noel, G.Shu, and B.B. Blinov. Hyperfine and optical barium ion qubits. *Physical Revie A 81, 052328*, 2010.

[11] Daniela Dragoman and Mircea Dragoman. *Quantum-Classical Analogies.* Springer.

[12] Laird Nicholas Egan. Scaling quantum computers with long chains of trapped ions. *University of Maryland*, 2021.

[13] Christopher J. Foot. *Atomic Physics.* Oxford University Press, 2005.

[14] J. P Gaebler, C.H. Baldwin, S. A. Moses, J. M. Dreiling, C. Figgatt, M. Foss-Feig, D. Hayes, and J. M. Pino. Suppression of mid-circuit measurement crosstalk errors with micromotion. 2022.

[15] P.C. Haljan, K.-A. Brickman, L.Deslauriers, P.J.Lee, and C.Monroe. Spin-dependent forces on trapped ion s for phase-stable quantum gates and entangled states of spin and motion. 2005.

[16] Maximilian Josef Harlander. Architecture for a scalable ion-trap quantum computer. *University of Innsbruck*, 2012.

[17] Winfried K. Hensinger. Quantum computer based on shuttling trapped ions. *Nature*, 2021.

[18] Jonathon P. Home. Quantum science and metrology with mixed-species ion chains. *ETH Zurich*, 2020.

[19] Kenneth Earl Wright II. Manipulation of the quantum motion of trapped atominc ions via stimulated raman transitions. *University of Maryland, College Park*, 2017.

[20] Ismail Volkan Inlek. *Multi-Species Trapped Atomic Ion Modules for Quantum Networks.* PhD thesis, University of Maryland, 2016.

[21] Daniel F. V. James. Quantum dynamics of cold trapped ions, with application to quantum computation. 1997.

[22] J.M.Pino and et. al. Demonstration of the trapped-ion quantum ccd computer architecture. 2021.

[23] Henning Kalis, Frederick Hakelberg, Matthias Wittemer, Manuel Mielenz, Ulrich Warring, and Tobias Schaetz. Motional-mode analysis of trapped ions. 2018.

[24] V. Kaushal, B. Lekitsch, A. Stahl, J. Hilder, D. Pijn, C. Schmiegelow, A. Bermudez, M. M:uller, F. Schmidt-Kaler, and U. Poschinger. Shuttling-based trapped-ion quantum information processing. 2019.

[25] K. A. Landsman, Y. Wu, P. H. Leung, D. Zhu, N. M. Linke, K. R. Brown, L. Duan, and C. Monroe. Two-qubit entangling gates within arbitrarily long chains of trapped ions. 2019.

[26] Kevin Antony Landsman. Construction, optimization, and applications of a small trapped-ion quantum computer. *University of Maryland, College Park*, 2019.

[27] Patricia J. Lee. *Quantum Information Processing with Two Trapped Cadmium Ions.* PhD thesis, University of Maryland, 2006.

[28] Pei Jiang Low. Tolerable experimental imperfections for a quadrupole blade ion trap and practical qudit gates with trapped ions. Master's thesis, University of Waterloo, 2019.

[29] Pei Jiang Low, Brendan M. White, Andrew A. Cox, Matthew L. Day, and Crystal Senko. Practical trapped-ion protocols for universal qudit-based quantum computing. *Phys. Rev. Research 2, 033128*, 2020.

[30] Timothy Andrew Manning. Quantum information processing with trapped ion chains. *University of Maryland, College Park*, 2014.

[31] Matteo Marinelli. Quantum information processing with mixed-species ion crystals. *ETH Zurich*, 2020.

[32] Klaus Mølmer and Anders Sørensen. Quantum computation with ions in thermal motion. 1999.

[33] G. Morigi and H. Walther. Two-species coulomb chains for quantum inforamtion. *The European Physical Journal D*, 2000.

[34] H.C Nagerl, D. Leibfried, F. Schmidt-Kaler, J. Eschner, and R. Blatt. Coherent excitation of normal modes in a string of $Ca^+$ ions. 1998.

[35] V. Nebendahl, H. Haffner, and C.F. Roos. Optimcal control of entangling operations for trapped-ion quantum computing. *Physical Review A 79, 012312*, 2009.

[36] M.A. Nielson and I.L. Chuang. *Quantum Computation and Quantum Information.* Cambridge University Press, 2000.

[37] Elijah Pelofske, Andreas Brtschi, and Stephan Eidenbenz. Quantum volume in practice: What users can expect from nisq devices. 2022.

[38] Manas Sajjan. Experimental and theoretical investigations of radio-frequency and optical trapping potentials for atomic ions. *University of Waterloo*, 2020.

[39] Crystal Senko. Dynamics and excited states of quantum many-body spin chains with trapped ions. *University of Maryland, College Park*, 2014.

[40] Ding ShengChao and Jin Zhi. Review on the study of entanglement in quantum computation speedup. *Chinese Science Bulletin*, 2007.

[41] K-A Brickman Soderberg and C Monroe. Phonon-mediated entanglement for trapped ion quantum computing. *Rep. Prog. Phys. 73*, 2009.

[42] K. Sosnova, A. Carter, and C. Monroe. The character of motional modes for entanglement and sympathetic cooling of mixed-species trapped ion chains. *Phys. Rev. A 103, 012610*, 2021.

[43] Ksenia Sosnova. Mixed-species ion chains for quantum networks. *University of Maryland*, 2020.

[44] Andrew Steane. Quantum computing. *Rep.Prog.Phys. 61*, 1998.

[45] Ting Rei Tan. High-fidelity entangling gates with trapped-ions. *University of Colorado*, 2016.

[46] Yi Hong Teoh. Machine learning and optimization techniques for trapped-ion quantum simulators. *University of Waterloo*, 2020.

[47] Yi Hong Teoh, Manas Sajjan, Zewen Sun, Fereshteh Rajabi, and Rajibul Islam. Manipulating phonons of a trapped-ion system using optical tweezers. *Phys. Rev. A 104, 022420*, 2021.

[48] Brendan M. White, Pei Jiang Low, Yvette de Sereville, Matthew L. Day, Noah Greenberg, Richard Rademacher, and Crystal Senko. Isotope-selective laser ablation ion-trap loading of $^{137}\mathrm{Ba}^+$ using a $\mathrm{BaCl}_2$ target. *Physical Review A*, 2022.

[49] Colin P. Williams. *Explorations in Quantum Computing*. Springer, 2011.

[50] John Albert Wright. Mixed species ion chains for scalable quantum computation. *University of Washington*, 2015.

# APPENDICES

# Appendix A

# Hamiltonian Derivation: Bi-chromatic Laser Applied to an Ion Chain

This is the derivation upon which the MS gate derivation is dependent in Chapter 2. In other words, the MS Hamiltonian upon which the MS unitary operator is calculated will be derived here.

Starting with the Hamiltonian for a monochromatic laser interacting with a qubit (ion) confined to a harmonic potential, where $\omega_q$ is the qubit frequency, $\omega$ is the laser frequency, $\omega_m$ is the motional frequency and the operators are defined in the standard way:

$$H = \frac{\omega_q}{2}\sigma_z + \omega_m a^\dagger a + \Omega \cos(kx_0(a + a^\dagger) - \omega t + \phi)\sigma_x \tag{A.1}$$

where

$$H_0 = \frac{\omega_q}{2}\sigma_z + \omega_m a^\dagger a \tag{A.2}$$

Transforming the Hamiltonian, $H$, into the interaction picture with respect to $H_0$:

$$H_{int} = e^{H_0 t}(H - H_0)e^{-H_0 t} \tag{A.3}$$

By substituting the relevant values for $H_0$ and $H$:

$$H_{int} = e^{\frac{i\omega_q}{2}} e^{i\omega_m t a^\dagger a} \frac{\Omega}{2}(e^{ikx_0(a+a^\dagger)} e^{-i\omega t + i\phi} + e^{-ikx_0(a+a^\dagger)} e^{i\omega t - i\phi}) \tag{A.4}$$

By using the Baker-Hausdorff lemma to simplify:

$$H_{int} = \frac{\Omega}{2}[\sigma_{+}\exp(i(\eta(ae^{-i\omega_m t}+a^{\dagger}e^{i\omega_m t})-\delta t+\phi))+\sigma_{-}\exp(-i(\eta(ae^{-i\omega_m t}+a^{\dagger}e^{i\omega_m t})-\delta t+\phi))] \tag{A.5}$$

By applying the Lamb-Dicke approximation:

$$e^{i\eta} \simeq 1 + i\eta \tag{A.6}$$

and defining:

$$\alpha(t) = a\exp(-i\omega_m t) + a^{\dagger}\exp(i\omega_m t) \tag{A.7}$$

the interaction Hamiltonian simplifies to:

$$H_{int} = \frac{\Omega}{2}\sigma_{+}(1+i\eta\alpha)e^{i(-\delta t+\phi)} + \frac{\Omega}{2}\sigma_{-}(1-i\eta\alpha)e^{-i(-\delta t+\phi)} \tag{A.8}$$

Applying this derivation to the specific experimental MS entangling scheme whereby two incident laser beams both equally and oppositely detuned, $\pm\mu$, are incident on the ions and using a rotating wave approximation (RWA), the red and blue sideband Hamiltonians, $H_r$ and $H_b$ are as follows:

$$H_r = \frac{\Omega}{2}\sigma_{+}(1+i\eta(ae^{-i\omega_m t}+a^{\dagger}e^{i\omega_m t}))e^{i\mu t}e^{i\phi_r}+\frac{\Omega}{2}\sigma_{-}(1-i\eta(ae^{-i\omega_m t}+a^{\dagger}e^{i\omega_m t}))e^{-i\mu t}e^{-i\phi_r} \tag{A.9}$$

$$H_b = \frac{\Omega}{2}\sigma_{+}(1+i\eta(ae^{-i\omega_m t}+a^{\dagger}e^{i\omega_m t}))e^{i\mu t}e^{i\phi_b}+\frac{\Omega}{2}\sigma_{-}(1-i\eta(ae^{-i\omega_m t}+a^{\dagger}e^{i\omega_m t}))e^{-i\mu t}e^{-i\phi_b} \tag{A.10}$$

The spin-dependent force occurs when both the blue and red sidebands act on the ion simultaneously, resulting in a spin-dependent force Hamiltonian, $H_{SDF}$:

$$\begin{aligned} H_{SDF} = {} & \frac{\Omega}{2}\sigma_{+}(1+i\eta(ae^{-i\omega_m t}+a^{\dagger}e^{i\omega_m t}))(e^{i\mu t}e^{-i\phi_r}+e^{-i\mu t}e^{-i\phi_b})+ \\ & \frac{\Omega}{2}\sigma_{-}(1-i\eta(ae^{-i\omega_m t}+a^{\dagger}e^{i\omega_m t}))(e^{-i\mu t}e^{-i\phi_r}+e^{i\mu t}e^{-i\phi_b}) \end{aligned} \tag{A.11}$$

Applying another RWA, thus ignoring terms oscillating at $(\mu + \omega_m)$ and defining $\phi_m = (\phi_r + \phi_b)/2$ and $\phi_s = (\phi_r + \phi_b + \pi)/2$, the spin-dependent force Hamiltonian then simplifies to:

$$H_{SDF} = \frac{\eta\Omega}{2}(\sigma_+ e^{i\phi_s} + \sigma_- e^{-i\phi_s})(a e^{i(\mu-\omega_m)t+i\phi_m} + a^\dagger e^{-i(\mu-\omega_m)t-i\phi_m}) \tag{A.12}$$